ARTICLES
https://doi.org/10.1038/s41556-020-00605-6
nature cell biology

Check for updates

# Nuclear F-actin counteracts nuclear deformation and promotes fork repair during replication stress

Noa Lamm[1], Mark N. Read[2], Max Nobis[3], David Van Ly[1,4], Scott G. Page[1], V. Pragathi Masamsetti[1], Paul Timpson[3], Maté Biro[5] and Anthony J. Cesare[1]✉

**Filamentous actin (F-actin) provides cells with mechanical support and promotes the mobility of intracellular structures. Although F-actin is traditionally considered to be cytoplasmic, here we reveal that nuclear F-actin participates in the replication stress response. Using live and super-resolution imaging, we find that nuclear F-actin is polymerized in response to replication stress through a pathway regulated by ATR-dependent activation of mTORC1, and nucleation through IQGAP1, WASP and ARP2/3. During replication stress, nuclear F-actin increases the nuclear volume and sphericity to counteract nuclear deformation. Furthermore, F-actin and myosin II promote the mobility of stressed-replication foci to the nuclear periphery through increasingly diffusive motion and directed movements along the nuclear actin filaments. These actin functions promote replication stress repair and suppress chromosome and mitotic abnormalities. Moreover, we find that nuclear F-actin is polymerized in vivo in xenograft tumours after treatment with replication-stress-inducing chemotherapeutic agents, indicating that this pathway has a role in human disease.**

Hindrances to DNA replication are collectively termed replication stress[1]. Cells mitigate such threats through the replication stress response, which is regulated by the ATR kinase[2]. ATR coordinates cell-cycle arrest and nuclear activities that promote the stability, repair and restart of arrested replication forks[3]. During replication stress, cells must cope with spatial and structural challenges, including coordinating fork repair throughout the nucleus[4] and resolving torsional stress in chromatin attached to the nuclear periphery[5].

The actin cytoskeleton underpins cell shape control, motility and cargo transport, which are chiefly regulated through the spatiotemporally controlled polymerization of monomeric actin into F-actin[6]. Although actin is mostly cytoplasmic, transient F-actin occurs within nuclei[7] and functions in the serum response[8], cell spreading[9], mitotic exit[10] and homology-directed double-stranded-break (DSB) repair[11–13]. mTOR is an atypical serine–threonine kinase in the phosphatidylinositol 3-kinase related family[14]. mTOR complex 1 (mTORC1) and 2 (mTORC2) share the mTOR catalytic subunit but differ in accessory subunits and substrate specificity[15]. Among its functions, mTOR regulates the rearrangement of the actin cytoskeleton through the Wiskott–Aldrich syndrome protein (WASP) family[16,17], which in turn controls the actin related protein 2 and actin related protein 3 (ARP2/3) actin-nucleating complex[18].

F-actin was implicated in DNA replication through the recruitment of pre-initiation complex subunits during G1 phase[19]. However, whether dynamic rearrangement of the nuclear cytoskeleton occurred during S phase, or whether actin or mTOR participated in the replication stress response remains unclear[20]. In this Article, we demonstrate that, in response to replication stress, ATR and mTORC1 regulate WASP and ARP2/3-dependent nuclear F-actin polymerization to alter nuclear architecture, enable the mobility of stressed-replication foci and promote replication stress repair.

## Results

**Replication stress induces nuclear F-actin.** We induced replication stress by treating human cell cultures with moderate doses of the DNA polymerase inhibitor aphidicolin (APH, 0.4 μM) or the ribonucleotide reductase inhibitor hydroxyurea (HU, 500 μM). Super-resolution imaging through the nuclear mid-plane of phalloidin-stained asynchronous primary IMR90 fibroblasts revealed significant increases in nuclear F-actin$^+$ cells in APH- or HU-treated cultures (Fig. 1a,b). Specific visualization of endogenous nuclear actin with a nuclear localization signal (NLS) and GFP-tagged chromobody (hereafter, nuclear-actin-CB)[9] also revealed an increase in F-actin$^+$ nuclei in asynchronous APH- or HU-treated IMR90, IMR90 expressing HPV16 E6 and E7 (IMR90$^{E6E7}$), or U-2OS osteosarcoma cultures (Extended Data Fig. 1a–d). Similarly, in vitro pyrene actin assays[8] revealed an increase in the rate of actin polymerization in nuclear extracts from APH-treated cells (Fig. 1c and Extended Data Fig. 1e–g). To determine whether APH conferred an S-phase-specific response, we coexpressed nuclear-actin-CB with an red fluorescent protein (RFP)-tagged Proliferating cell nuclear antigen (PCNA) chromobody (hereafter, PCNA-CB). Punctate PCNA-CB foci demarcate sites of active DNA replication and serve as a specific S-phase marker[21]. Consistent with a replication stress response, APH induced a dose-dependent increase in F-actin$^+$ S-phase nuclei (Fig. 1d,e).

Visualizing the dynamics of F-actin required effective live-cell and nuclear-specific actin imaging (Supplementary Videos 1 and 2). We compared spinning-disk confocal live imaging of cells expressing nuclear-actin-CB with cells exogenously expressing NLS- and far-red-tagged actin monomers (3×NLS-actin-miRFP670 (hereafter, nuclear-WT-actin))[11]. Coexpression of nuclear-actin-CB and nuclear-WT-actin revealed that nuclear-actin-CB marked thick actin bundles but not the finer actin network that was identified by

[1]Genome Integrity Unit, Children's Medical Research Institute, University of Sydney, Westmead, New South Wales, Australia. [2]School of Computer Science, The Westmead Initiative and The Charles Perkins Centre, University of Sydney, Camperdown, New South Wales, Australia. [3]The Garvan Institute of Medical Research, St Vincent's Clinical School, Faculty of Medicine, University of New South Wales, Sydney, New South Wales, Australia. [4]School of Medicine, The University of Notre Dame Australia, Sydney, New South Wales, Australia. [5]EMBL Australia, Single Molecule Science node, School of Medical Sciences, University of New South Wales, Sydney, New South Wales, Australia. ✉e-mail: tcesare@cmri.org.au

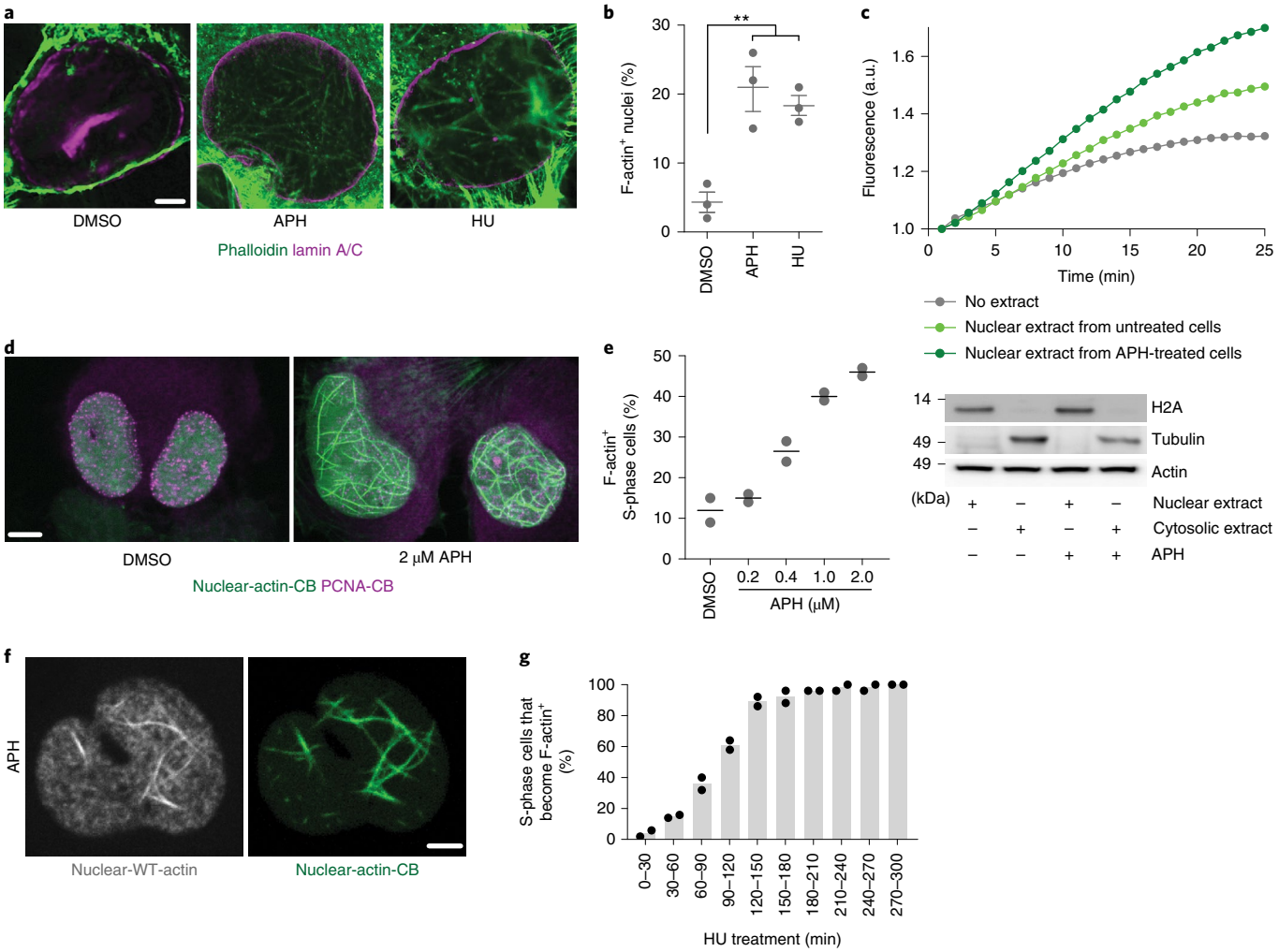


**Fig. 1 | Replication stress induces S-phase nuclear F-actin. a**, Super-resolution Airyscan microscopy of a single *z* plane from U-2OS cells that were stained with phalloidin and anti-lamin A/C antibodies after treatment with dimethyl sulfoxide (DMSO), 0.4 μM APH or 500 μM HU for 24 h. **b**, The frequency of F-actin+ nuclei from the experiments shown in **a**. Data are mean ± s.e.m. $n = 3$ biological replicates, scoring ≥23 nuclei per replicate. Statistical analysis was performed using two-sided Fisher's exact tests; $^{**}P < 0.01$. **c**, Normalized timecourse of pyrene-labelled actin assembly in the presence or absence of IMR90 nuclear extracts (top). One of three independent biological replicates is shown. Bottom, western blots of nuclear and cytosolic extracts used in the above experiment from cells with or without 0.4 μM APH for 8 h. The loaded volume of nuclear to cytoplasmic extract is 5:1. a.u., arbitrary units. **d**, Fixed images of nuclear-actin-CB- and PCNA-CB-expressing S-phase cells that were treated with vehicle or 2 μM APH for 24 h. **e**, Quantification of F-actin+ S-phase cells in cultures that were treated with or without APH for 24 h. $n = 2$ biological replicates, assaying ≥36 nuclei per replicate. The points represent replicate means and the lines show the experimental mean. **f**, Still images from live-cell microscopy of U-2OS cells coexpressing nuclear-WT-actin and nuclear-actin-CB that were treated with 0.4 μM APH. **g**, Quantification of the time to S-phase nuclear F-actin positivity in U-2OS cells expressing nuclear-WT-actin after administration of 2 mM HU. $n = 2$ biological replicates, analysing ≥40 cells per replicate. The points represent replicate means and the bars represents the experimental mean. For **a**, **d** and **f**, scale bars, 5 μm. Source data are available online.

nuclear-WT-actin (Fig. 1f). Visualization of nuclear F-actin through nuclear-actin-CB also failed to label some phalloidin-stained fibres (Extended Data Fig. 1h). Although nuclear-actin-CB labelled F-actin with delayed kinetics compared with nuclear-WT-actin, both strategies showed S-phase nuclear actin disassembly when APH was washed from the culture medium (Extended Data Fig. 1i,j). Furthermore, we assayed the temporal dynamics of nuclear F-actin formation in nuclear-WT-actin-expressing cells that were treated with 2 mM HU. Under 2 mM HU, replication stress is reversible for at least the first 4 h, while longer incubation periods induce fork collapse[22]. With 2 mM HU, 89% of the S-phase cells that exhibited nuclear F-actin did so within the first 2.5 h of treatment (Fig. 1g), consistent with actin polymerization occurring concurrently with fork stalling and before fork collapse.

We note that cells expressing nuclear-WT-actin revealed nucleolar F-actin after treatment with APH, whereas nucleolar signals were not observed in nuclear-actin-CB-expressing cells or with phalloidin staining alone (Extended Data Fig. 1k). Nucleolar F-actin may represent a bona fide response; however, the nature of these signals remains undefined. As nuclear-actin-CB did not impact nuclear actin levels (Extended Data Fig. 1l), and previous studies indicate that the chromobody does not induce spurious phenotypes[8,10,12], we used nuclear-actin-CB for live-cell imaging.

**Replication stress activates mTORC1.** Induction of S-phase nuclear F-actin with replication stress suggested that it is regulated through ATR (Supplementary Video 2). We hypothesized that mTOR may also have a role[20]. mTOR regulates actin polymerization, and both

mTOR and F-actin are linked to tolerance of genomic damage in yeast[23,24]. Furthermore, mTOR is a potential ATR substrate[25,26], and mTOR is activated by IPMK[27], which is coregulated with ATR after DSB induction[28]. As expected, APH induced ATR-dependent phosphorylation of its effector CHK1 (Extended Data Fig. 2a). APH or HU also increased the phosphorylation of mTOR and the mTORC1 effectors P70S6 and 4EBP1, whereas the mTORC2 effectors PKCα/β and AKT[15] were only mildly affected (Fig. 2a,b and Extended Data Fig. 2a). IPMK depletion suppressed increased mTORC1 signalling in response to APH (Fig. 2c and Extended Data Fig. 2b).

We assessed the potential connectivity between ATR and mTOR using selective chemical inhibitors. Treating cells with APH and 100 nM of the ATR inhibitor VE-822 suppressed CHK1 phosphorylation as well as the increased mTOR signalling that is induced by replication stress (Fig. 2b and Extended Data Fig. 2a). By contrast, 200 nM of the mTOR inhibitor INK128 (ref. [29]) suppressed mTOR signalling with APH but did not affect CHK1 phosphorylation (Fig. 2b and Extended Data Fig. 2a). Importantly, 100 nM VE-822 did not suppress mTOR activation or mTORC1 signalling induced by the metabolic activator insulin-like growth factor 1 (Fig. 2d)[30]. VE-822 therefore did not directly inhibit mTOR under our experimental conditions. Thus, replication stress activates mTORC1 in an ATR- and IPMK-dependent manner.

**The replication-stress-induced nuclear F-actin pathway.** IQGAP1 associates with mTORC1 (ref. [31]), stabilizes actin bundles[32], stimulates F-actin polymerization through WASP and ARP2/3 (ref. [33]) and is imported into the nucleus during replication stress[34]. We observed that IQGAP1 localized to nuclear F-actin bundles in APH-treated S-phase cells (Extended Data Fig. 2c). Furthermore, LIM kinase (LIMK) phosphorylates Ser 3 of cofilin 1 to inhibits cofilin 1 from severing actin filaments[35]. Consistent with an F-actin-promoting environment, we found a subtle increase in the phosphorylation of Ser 3 of cofilin 1 after APH treatment (Extended Data Fig. 2d).

We treated asynchronous nuclear-actin-CB- and PCNA-CB-expressing cells with APH in the presence or absence of the actin-polymerization inhibitor latrunculin B (LatB), VE-822, INK128, the WASP inhibitor wiskostatin, the ARP2/3 inhibitor CK-666 or the LIMK inhibitor LIMKi 3 (Fig. 2e, Extended Data Fig. 2e, and Supplementary Videos 3 and 4). We observed that APH induced nuclear F-actin specifically during S phase, dependent on actin polymerization, ATR, mTOR, WASP, ARP2/3 and LIMK activity (Fig. 2f and Extended Data Fig. 3a–c). Inhibiting mTOR or ATR also induced a rare phenotype in APH-treated cells in which nuclear F-actin briefly assembled before losing structural integrity (Extended Data Fig. 2e and Supplementary Video 5). Similarly, depleting ATR, mTOR, ARP2/3 or IQGAP1 also suppressed the induction of S-phase nuclear F-actin by APH (Extended Data Fig. 3d–g). Consistent with mTORC1-specific signalling, depleting the mTORC1 subunit RPTOR supressed S-phase nuclear F-actin in APH-treated cells, whereas depleting the mTORC2 subunit RIPTOR did not (Extended Data Fig. 3f,g). Consistent with ARP2/3-mediated actin nucleation, we observed ~70° branching in the nuclear F-actin network after APH treatment (Extended Data Fig. 3h).

Furthermore, we found that S-phase nuclear volume and sphericity increased with APH treatment (Fig. 2g,h). These changes in nuclear architecture were suppressed by pharmacological inhibition or short interfering RNA (siRNA) depletion of ATR, mTOR, WASP, ARP2/3 or LIM kinase (Fig. 2g,h and Extended Data Fig. 3i,j).

**Nuclear-specific F-actin alters the nuclear architecture.** F-actin-dependent alteration of the nuclear architecture suggested that nuclear-specific actin forces may drive these structural changes. To investigate nuclear specificity, we expressed nuclear-WT-actin or polymerization-deficient R62D mutant actin tagged with a NLS and a far red fluorescent protein (3×NLS-actinR62D-miRFP670 (hereafter, nuclear-mutant-actin))[11] (Fig. 3a). We also depleted importin 9 (IPO9) to reduce the nuclear pool of endogenous actin monomers[36] and expressed nuclear-actin-CB to visualize endogenous nuclear F-actin (Fig. 3a,b).

After APH treatment, there was a significant reduction in F-actin$^+$ S-phase nuclei in the nuclear-mutant-actin-expressing cells compared with the nuclear-WT-actin-expressing cells (Fig. 3c). This was further exacerbated after IPO9 depletion (Fig. 3c). Nuclear-mutant-actin expression with IPO9 depletion also suppressed APH-induced changes in nuclear volume and sphericity (Fig. 3d,e). Cytoplasmic F-actin was present in nuclear-mutant-actin-expressing cells, indicating that actin polymerization was specifically inhibited within the nucleus (Fig. 3f). Moreover, we observed that the increase in nuclear volume during S-phase after treatment with APH corresponded temporally to the presence of nuclear F-actin (Fig. 3g). We also found that LatB and INK128 did not affect the nuclear levels of IQGAP1, ARP2/3 or actin (Fig. 3h). This indicated that LatB and INK128 did not suppress the APH-induced changes in the nuclear architecture by altering the nuclear abundance of key pathway components.

**Stressed-replication foci associate with nuclear F-actin.** FANCD2 localizes to stalled replication forks in cytologically detectable punctate foci[37]. By contrast, RAD51 colocalizes in punctate replication foci only when a fork has collapsed into a DSB[22]. S-phase timing can be determined on the basis of PCNA focus size and distribution[21] (Extended Data Fig. 4a). PCNA-CB foci commonly colocalized with FANCD2 and nuclear F-actin in late-S-phase APH-treated cells (Fig. 4a and Extended Data Fig. 4b,c). By contrast, in early-S-phase APH-treated cells, FANCD2 localized to a small proportion of PCNA-CB foci, indicating that only a subset of

**Fig. 2 | Replication-stress-induced nuclear F-actin alters the nuclear architecture through a pathway that is regulated by ATR, mTORC1, IQGAP1, WASP, ARP2/3 and LIM kinase. a**, Western blot analysis of whole-cell extracts from U-2OS and IMR90 cells that were treated with 0.4 μM APH or 500 μM HU for 8 h. Quantification of the signal of mTOR phosphorylated at Ser 2448 (mTOR-S2448) normalized to total mTOR and relative to the DMSO controls is shown below in arbitrary units. Data are mean ± s.e.m. $n = 3$ biological replicates. **b**, Western blot analysis of whole-cell extracts from HT1080 6TG cells that were treated with 0.4 μM APH for 8 h with or without 100 nM VE-822 or 200 nM INK128. **c**, Western blot analysis of whole-cell extracts from siRNA-transfected HT1080 6TG cells treated with or without 0.4 μM APH for 8 h. Cells were siRNA transfected 48 h before extraction. **d**, Western blot analysis of whole-cell extracts from HT1080 6TG cells that were treated with 100 ng ml$^{-1}$ IGF-I with or without 100 nM μM VE-822 for 1 h. All blots are a representative example out of three biological replicates. **e**, Representative images from spinning-disk confocal live microscopy analysis of U-2OS cells expressing nuclear-actin-CB and PCNA-CB that were treated with DMSO or 0.4 μM APH with or without 200 nM LatB, 200 nM INK128, 100 nM VE-822, 200 μM CK-666, 5 μM wiskostatin or 10 μM LIMKi 3. Time is shown as hours:minutes relative to the first image of the series. Scale bar, 5 μm. **f**, The frequency of nuclear F-actin$^+$ S-phase nuclei from the experiments shown in **e**. Data are mean ± s.e.m. $n = 3$ biological replicates, scoring ≥51 nuclei per replicate. Statistical analysis was performed using two-sided Fisher's exact tests. **g**,**h**, Timecourses of normalized nuclear volume (**g**) and sphericity (**h**) from the experiment shown in **e**. Data are mean ± s.e.m. $n = 34$ (DMSO), $n = 36$ (APH), $n = 31$ (APH + LatB), $n = 31$ (APH + INK128), $n = 33$ (APH + VE-822), $n = 32$ (APH + CK-666), $n = 34$ (APH + wiskostatin) and $n = 31$ (APH + LIMKi 3) nuclei sampled from five biological replicates. Statistical analysis was performed using one-way analysis of variance. For **f**–**h**, $^{**}P < 0.01$, $^{****}P < 0.0001$. Source data are available online.

replication foci were stressed (Fig. 4a and Extended Data Fig. 4d). Similarly, with APH treatment, a small proportion of early-S-phase PCNA foci colocalized with nuclear F-actin. Notably, this small pool of F-actin-colocalized early-S-phase PCNA foci were also predominantly FANCD2 labelled (Fig. 4a and Extended Data Fig. 4d,e). Furthermore, only a minority of F-actin-associated PCNA foci were RAD51$^+$ (Extended Data Fig. 4b,c). PCNA foci therefore associate with nuclear F-actin as an attribute of stalled replication forks and not fork collapse.

In fixed images of APH-treated cells, we found that PCNA-CB foci localized with greater frequency to the nuclear periphery, dependent on actin polymerization, ATR and mTOR activity (Extended Data Fig. 4f,g). Difficult-to-replicate telomeric DNA[38] also localized to the nuclear periphery in APH-treated S-phase cells in an actin-polymerization-dependent manner (Extended Data Fig. 4h,i). We therefore examined the role of actin polymerization in replication focus mobility.

**F-actin promotes replication focus mobility.** To assay mobility, we developed analysis tools that register the nucleus location in progressive live-cell imaging frames to correct for cell motility (Supplementary Video 6). We limited the mobility analysis of

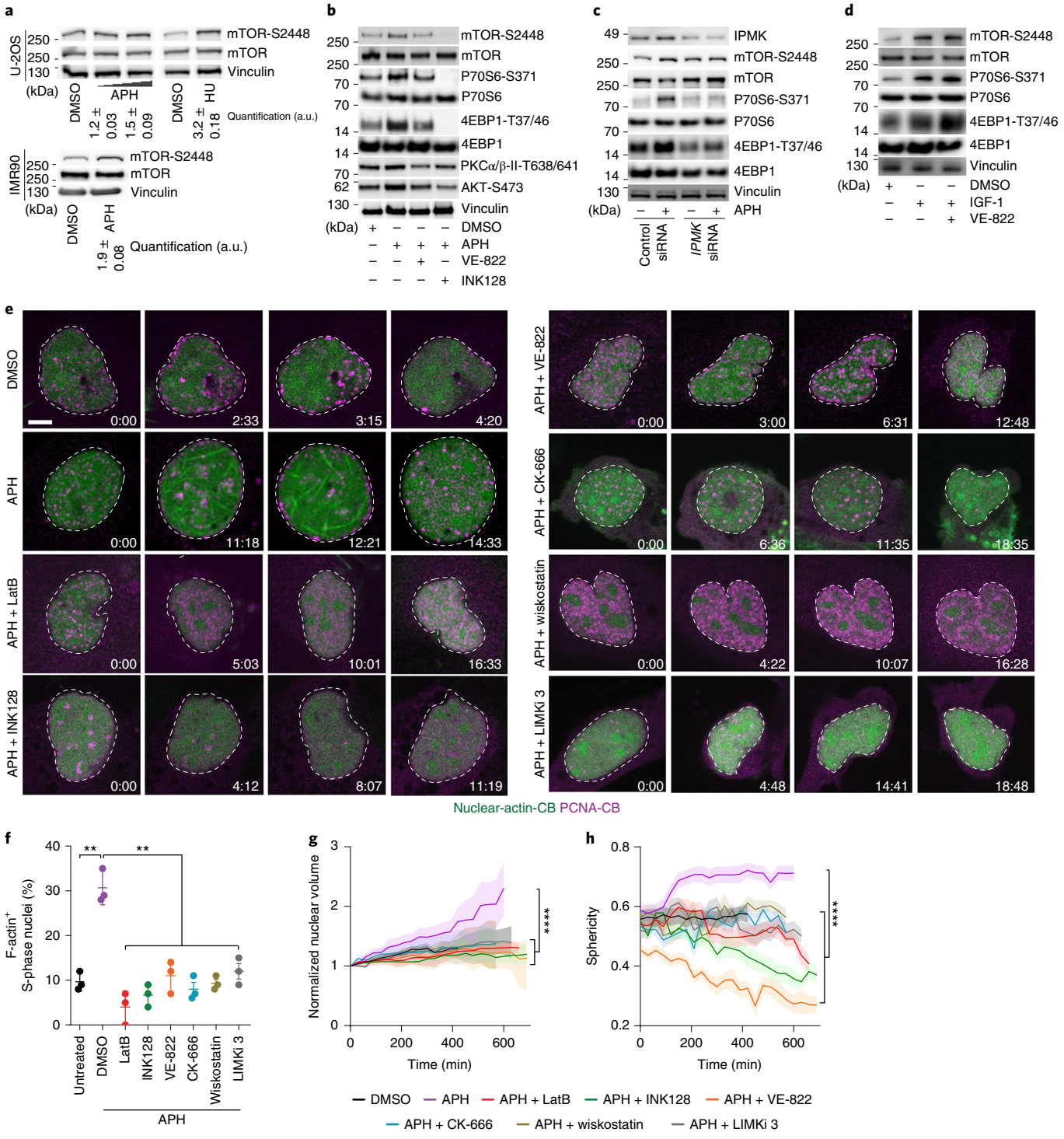

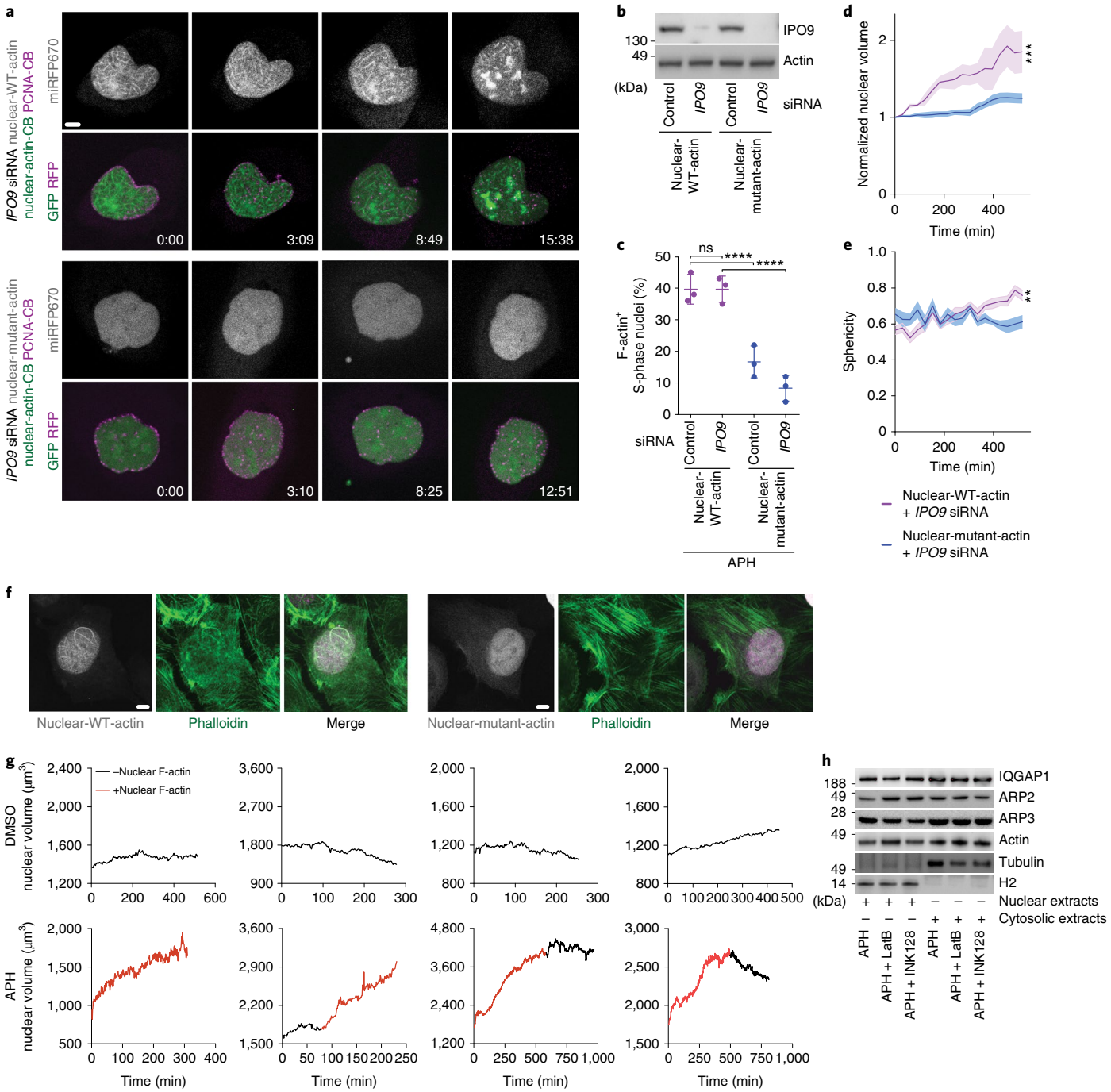


**Fig. 3 | Nucleus-specific F-actin alters the nuclear architecture during replication stress. a**, Still images from live-cell imaging of 0.4 μM APH treated U-2OS cells transfected with *IPO9* siRNA, which also express nuclear-actin-CB, PCNA-CB, and nuclear-WT-actin or nuclear-mutant-actin. Time is shown as hours:minutes relative to the first image. **b**, Western blots of whole-cell extracts from U-2OS cells transfected with nuclear-WT-actin or nuclear-mutant-actin, and control or *IPO9* siRNA. **c**, Quantification of S-phase cells that were double positive for miRFP670 and GFP-labelled nuclear F-actin in live-cell imaging of cultures treated with 0.4 μM APH. Data are mean ± s.e.m. $n = 3$ biological replicates, analysing ≥90 cells per replicate. Statistical analysis was performed using two-sided Fisher's exact tests. **d**,**e**, Quantification of normalized S-phase nuclear volume (**d**) and sphericity (**e**) in the cells treated with *IPO9* siRNA and APH from the experiments shown in **c**. Data are mean ± s.e.m. $n = 27$ nuclei per condition, sampled from two biological replicates. Statistical analysis was performed using one-way analysis of variance. **f**, Fixed images of nuclear-WT-actin- or nuclear-mutant-actin-transfected U-2OS cells that were treated with 0.4 μM APH and stained with phalloidin. **g**, Timecourse of the nuclear volume of S-phase U-2OS cells expressing nuclear-actin-CB and PCNA-CB in the presence or absence of 0.4 μM APH. Data were collected using spinning-disk confocal live imaging. Each graph represents the nuclear volume of an individual cell over a single S phase; the presence of nuclear-actin-CB labelled nuclear F-actin is indicated by the red colouration of the line. **h**, Western blot analysis of nuclear and cytosolic extracts from U-2OS cells that were treated with 0.4 μM APH with or without 200 nM LatB or 200 nM INK128 for 12 h. A representative experiment out of two experiments is shown. The loaded volume of nuclear to cytoplasmic extract is 5:1. For **a** and **f**, scale bars, 5 μm. For **c**–**e**, ns, not significant; $^{**}P < 0.01$, $^{***}P < 0.001$, $^{****}P < 0.0001$. For **a**, **b** and **f**, data are representative of three independent biological replicates. Source data are available online.

PCNA-CB-expressing cells to late S phase (Supplementary Videos 7 and 8). This was because late-S-phase PCNA-CB foci colocalized extensively with FANCD2, indicative of replication stress, and were fewer in number and trackable with automated methods (Fig. 4a,b and Extended Data Fig. 4c). From these data, we calculated the speed and mean-squared displacement (MSD) of PCNA-CB focus mobility (Extended Data Fig. 5a–c). APH increased the average velocity and MSD of late-replication focus movement, which was suppressed by LatB, INK128 or VE-822 (Extended Data Fig. 5a–c).

However, qualitative assessment suggested that there is heterogeneity in late S-phase PCNA-CB focus movements. To quantify this, we developed an analysis tool to perform sliding-window MSD calculations over the lifetime of a PCNA-CB focus from late-S-phase onset until S-phase resolution or nucleus escape from the imaging area. Focus movements were classified as confined (<0.8 MSD), diffusive (0.8–1.2 MSD), hyperdiffusive (>1.2 MSD, that is, directed mobility) or sustained hyperdiffusive (>1.2 MSD for five consecutive analysis windows, that is, sustained directed mobility). The data are presented as heat maps showing the temporal mobility of each PCNA-CB focus in an exemplar late-S-phase (Fig. 4c), and the collective mobility of all of the foci from multiple cells within an experimental condition (Fig. 4d). The results show that, after treatment with APH, late-S-phase PCNA-CB foci primarily displayed confined motility, punctuated by bursts of diffusive and directed mobility that were inhibited by LatB, VE-822 or INK128 (Fig. 4c,f).

To quantify the directionality of PCNA-CB focus mobility, we mitigated the influence of nuclear movements by limiting analysis to cells in which a mobile PCNA-CB focus relative to the nuclear periphery overlapped temporally with stationary PCNA-CB foci (Fig. 4e). These data show that APH induced PCNA-CB focus displacement towards the nuclear boundary, which was suppressed by treatment with LatB, VE-822 or INK128 (Fig. 4f).

**Replication foci move along nuclear F-actin.** Visual assessment revealed PCNA-CB focus movements along nuclear F-actin (Fig. 4e and Supplementary Video 9). Within the sliding-window MSD analysis dataset, 59% of hyperdiffusive PCNA-CB movements corresponded to foci sliding along nuclear F-actin, with an additional 29% of events corresponding to PCNA foci moving towards and associating with F-actin (Fig. 4g and Extended Data Fig. 5d). Myosins are motor proteins that translocate along F-actin[39]. Class-II and -V myosins are cargo transporters that are found in human nuclei[40]. To assay the potential involvement of myosin, we co-treated nuclear-actin-CB- and PCNA-CB-expressing cells with APH and the myosin-II inhibitors 2,3-butanedione monoxime (BDM)[41] or blebbistatin[42], or the myosin V inhibitor MyoVin-I. None of the myosin inhibitors affected nuclear F-actin polymerization or the nuclear architectural changes observed after treatment with APH (Fig. 4h and Extended Data Fig. 5e,f). However, both myosin-II inhibitors reduced S-phase PCNA-CB focus mobility in APH-treated cultures, whereas the myosin-V inhibitor had no effect (Fig. 4i and Extended Data Fig. 5g,h). Therefore, myosin II but not myosin V promotes PCNA-CB focus mobility after replication stress. Whether other myosins are involved remains to be established.

**Nuclear F-actin promotes replication stress repair.** To determine the impact of nuclear F-actin on replication fork repair, we performed molecular combing assays. Cells were treated with APH for 3 h to induce replication stress, followed by APH washout and replication recovery (Fig. 5a). Inhibiting fork repair slows the recovery DNA replication rate after APH removal. Treating cells with LatB, VE-822 or INK128 during only the recovery period suppressed the recovery replication rate (Fig. 5b,c and Extended Data Fig. 6a,b). In agreement with the above pathway analysis, depleting IQGAP1 or RPTOR also suppressed the recovery replication rate, whereas depleting RIPTOR did not (Fig. 5d). Recovery replication rates were also suppressed by nuclear-mutant-actin expression and IPO9 depletion, indicating that nuclear-specific F-actin promotes replication fork repair (Fig. 5e).

In agreement, inhibiting actin polymerization conferred molecular and cellular outcomes that are consistent with unresolved replication stress. Specifically, replication stress response signalling remained active after APH washout if actin polymerization was inhibited during recovery with LatB (Fig. 5f,g). LatB also promoted chromosome fragility and increased S/G2-phase duration (Extended Data Fig. 6c–e). In a dose-dependent manner, LatB also induced concomitant increases in micronuclei and anaphase abnormalities that were additive with APH co-treatment, consistent with replication-stress-induced chromosome segregation errors[43] (Fig. 5h,i and Extended Data Fig. 6f,g).

**Replication stress induces nuclear F-actin in vivo.** To determine whether the identified pathway was engaged in vivo, we created a stable U-2OS cell line constitutively expressing nuclear-actin-CB and PCNA-CB (Fig. 6a). These cells displayed nuclear F-actin cables with APH treatment consistent with observations reported above in which transient chromobody expression was used (Fig. 6a,b). The cells were used to generate xenograft tumours that were visualized in live mice using longitudinal intravital microscopy through optical windows[44,45] (Fig. 6c). After administration of the replication-stress-inducing frontline chemotherapeutic agents HU or carboplatin[46,47], we observed an induction of S-phase nuclear F-actin polymerization within the xenograft tumours (Fig. 6d,e). Replication stress therefore induces nuclear F-actin polymerization in human cells in vivo in response to chemotherapeutic intervention.

**Fig. 4 | ATR, mTOR and F-actin promote the mobility of stressed-replication foci.** All data were collected from U-2OS cells expressing nuclear-actin-CB and PCNA-CB treated with or without DMSO, 0.4 μM APH, 200 nM LatB, 200 nM INK128, 100 nM VE-822, 10 mM BDM, 50 μM blebbistatin or 100 μM MyoVin-I. **a**, Single *z*-plane Airyscan images of cells treated with APH for 24 h before FANCD2 staining. Representative of three biological replicates. **b**, Maximum-intensity projection still images from spinning-disk confocal live microscopy (left). Right, PCNA-CB focus tracks from the video that is represented on the left. **c**,**d**, Sliding window MSD analysis of PCNA-CB foci. **c**, Exemplar data from a single cell. Each row represents a different PCNA-CB focus. Time is from late S-phase onset to S-phase completion or cell migration from the imaging window. **d**, Pooled data from multiple cells. $n = 49$ (APH), $n = 46$ (APH + LatB or INK128) and $n = 47$ (APH + VE-822) tracks for each condition, sampled from ≥4 nuclei. Statistical analysis was performed using $\chi^2$ tests. **e**, Still image from live imaging of an APH treated cell (top). Bottom, timecourse of three regions containing an F-actin associated PCNA-CB focus. **f**, Direction of late-S-phase PCNA-CB focus displacement. Data are mean ± s.e.m. $n = 27$ (DMSO), $n = 28$ (APH), $n = 29$ (APH + LatB), $n = 30$ (APH + INK128) and $n = 27$ (APH + VE-822) foci per condition, sampled from ≥10 nuclei. Statistical analysis was performed using Kruskal–Wallis tests. **g**, Diffusive or hyperdiffusive late-S-phase PCNA-CB focus movement in APH-treated cells relative to nuclear F-actin. $n = 22$ foci, sampled from 4 nuclei. **h**, Nuclear F-actin$^+$ S-phase cells. Data are mean ± s.e.m. $n = 3$ biological replicates scoring ≥30 nuclei per replicate. Statistical analysis was performed using unpaired two-tailed *t*-tests. **i**, Data from cells treated as described in **h** and analysed as described in **d**. $n = 49$ (APH), $n = 26$ (APH + BDM) and $n = 25$ (APH + blebbistatin or MyoVin-I) tracks for each condition sampled from ≥4 nuclei. Statistical analysis was performed using $\chi^2$ tests. For **a**, **b** and **e**, scale bars, 5 μm in the main images and 2 μm in the expanded regions. For **d**, **f**, **h** and **i**, $^*P < 0.05$, $^{***}P < 0.001$, $^{****}P < 0.0001$. Source data are available online.

## Discussion

Here we demonstrate that nuclear-specific actin polymerization has a role in the replication stress response. In the identified pathway, ATR regulates nuclear F-actin polymerization through mTORC1, IQGAP1, WASP and ARP2/3, with additional regulation by LIMK and cofilin 1. This pathway modulates the nuclear architecture and, with myosin II, increases the mobility of stressed-replication foci. During replication stress, nuclear F-actin counteracts nuclear envelope deformation and promotes replication stress repair. Furthermore, we show nuclear F-actin induction in vivo after administration of replication stress-inducing chemotherapeutic agents. Taken together, our observations reveal a replication stress response pathway with physiological relevance to genome stability, cellular function and human disease.

Multiple lines of evidence support that nuclear-specific F-actin provides integral functions in the replication stress response. Results were consistent with different replication-stress-inducing agents in multiple human primary and transformed cells. Nuclear

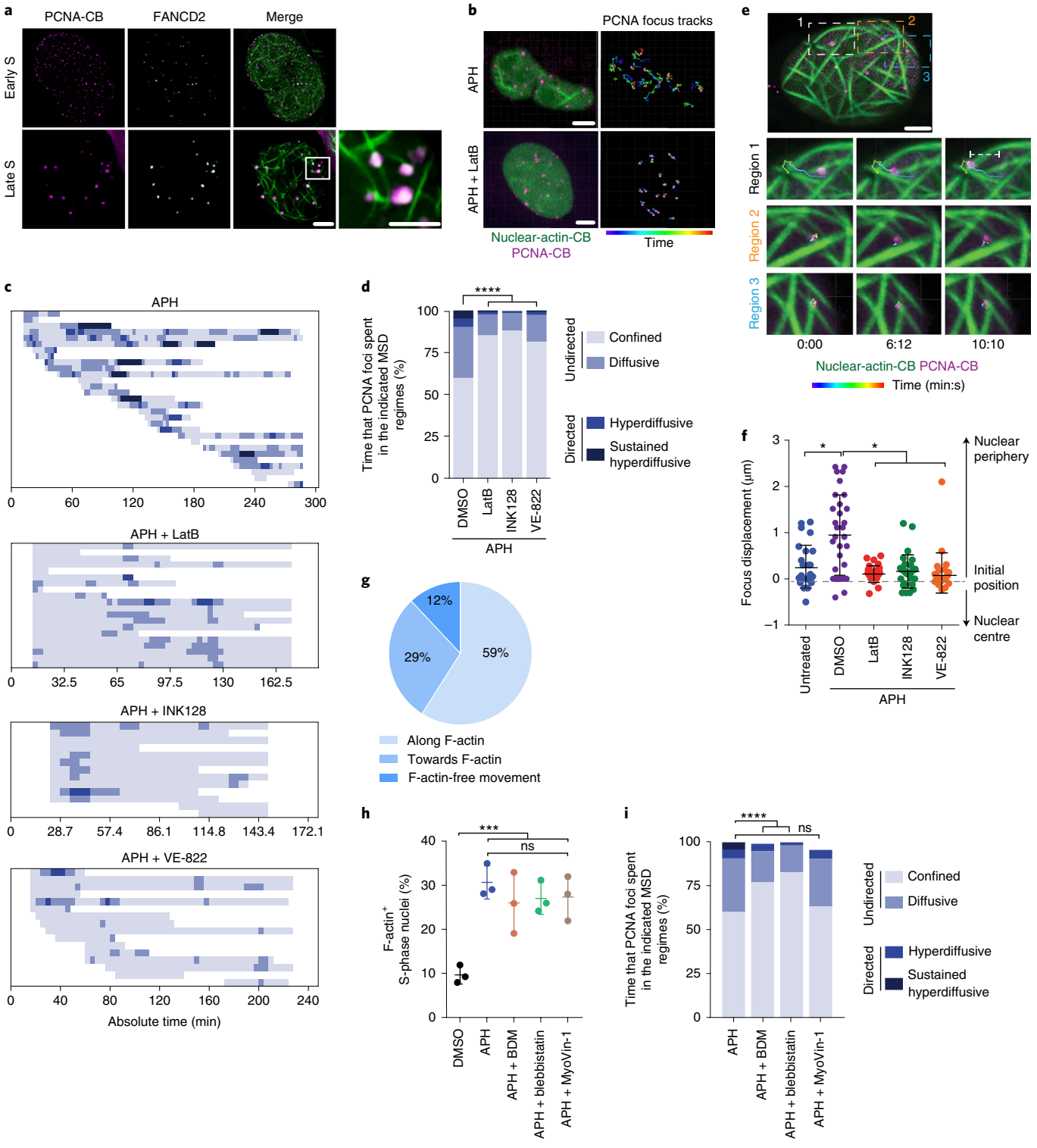

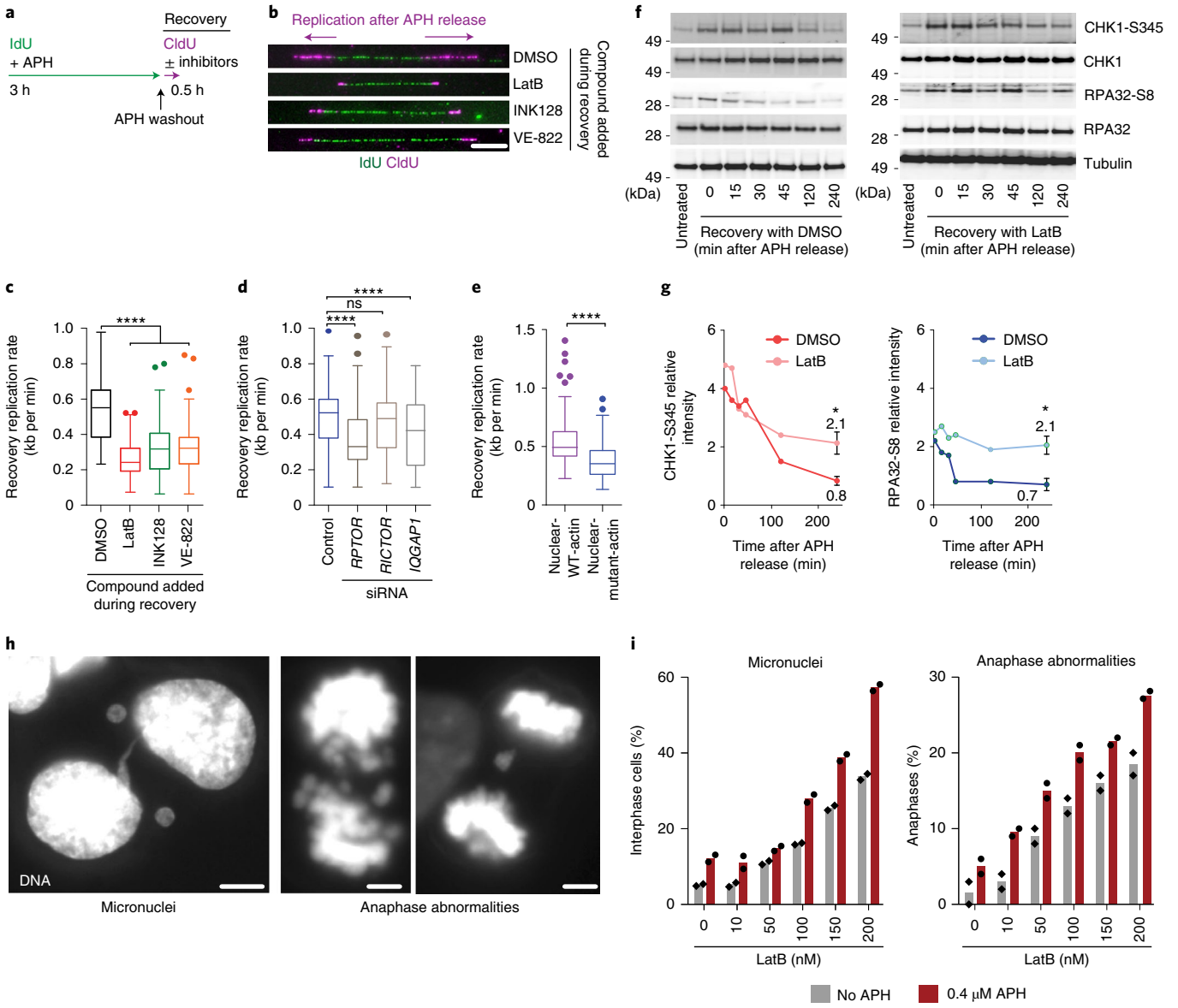


**Fig. 5 | Nuclear F-actin promotes replication stress repair. a**, The experimental timing to measure replication stress recovery in **b** and **c**. **b**, Molecular combing assays to measure the recovery replication rate in U-2OS cells after APH washout in the presence of DMSO, 200 nM LatB, 200 nM INK128 or 100 nM VE-822. Recovery replication rate is measured from the CldU track. Scale bar, 10 μm. **c**, The recovery replication rate in U-2OS cells treated with inhibitors as shown in **b**. $n = 132$ (DMSO), $n = 137$ (LatB), $n = 134$ (INK128) and $n = 136$ (VE-822) replication forks per condition, sampled from two biological replicates compiled into a Tukey box plot. Statistical analysis was performed using unpaired two-tailed *t*-tests. **d**, Recovery replication rate in siRNA-transfected U-2OS cells. $n = 127$ (control siRNA), $n = 107$ (*RPTOR* and *RICTOR* siRNA) and $n = 114$ (*IQGAP1* siRNA) replication forks per condition, sampled from two biological replicates compiled into a Tukey box plot. Statistical analysis was performed using unpaired two-tailed *t*-tests. **e**, The recovery replication rate in U-2OS cells transfected with *IPO9* siRNA and nuclear-WT-actin or nuclear-mutant-actin. $n = 171$ (nuclear-WT-actin) or $n = 164$ (nuclear-mutant-actin) replication forks per condition, sampled from two biological replicates compiled into a Tukey box plot. Statistical analysis was performed using unpaired two-tailed *t*-tests. **f**, Western blot analysis of whole-cell extracts from IMR90$^{E6E7}$ cells that were collected at the indicted time points after release from 24 h of treatment with 0.4 μM APH and then treated with or without 200 nM LatB. Representative blots from one out of three biological replicates are shown. **g**, Band intensity at the indicated time points from the blots shown in **f** relative to the untreated extract. The final time point is quantified. Data are mean ± s.e.m. $n = 3$ independent biological replicates. Statistical analysis was performed using unpaired two-tailed *t*-tests. **h**, Representative images of micronuclei (left) and anaphase abnormalities (middle and right) in LatB-treated U-2OS cells. Scale bars, 5 μm. **i**, The frequency of micronuclei and anaphase abnormalities from U-2OS cells treated with increasing dosages of LatB. $n = 2$ biological replicates, scoring ≥54 cells per replicate. For **c**–**e** and **g**, ns, not significant; $^{*}P < 0.05$, $^{****}P < 0.0001$. Source data are available online.

actin was polymerized with a moderate and sublethal dose of 0.4 μM APH[48] and dynamic F-actin polymerization and dissociation were observed in cells transiting the cell cycle without dying. Nuclear F-actin was therefore not a by-product of cell l ethality. Pharmacological replication stress promoted nuclear actin polymerization specifically during S phase and in a dose-dependent manner, and nuclear F-actin was dynamically reversed after removal of the replication-stress-inducing agent. We observed that stalled replication foci interacted with the nuclear cytoskeleton throughout S phase, and that nuclear F-actin was polymerized

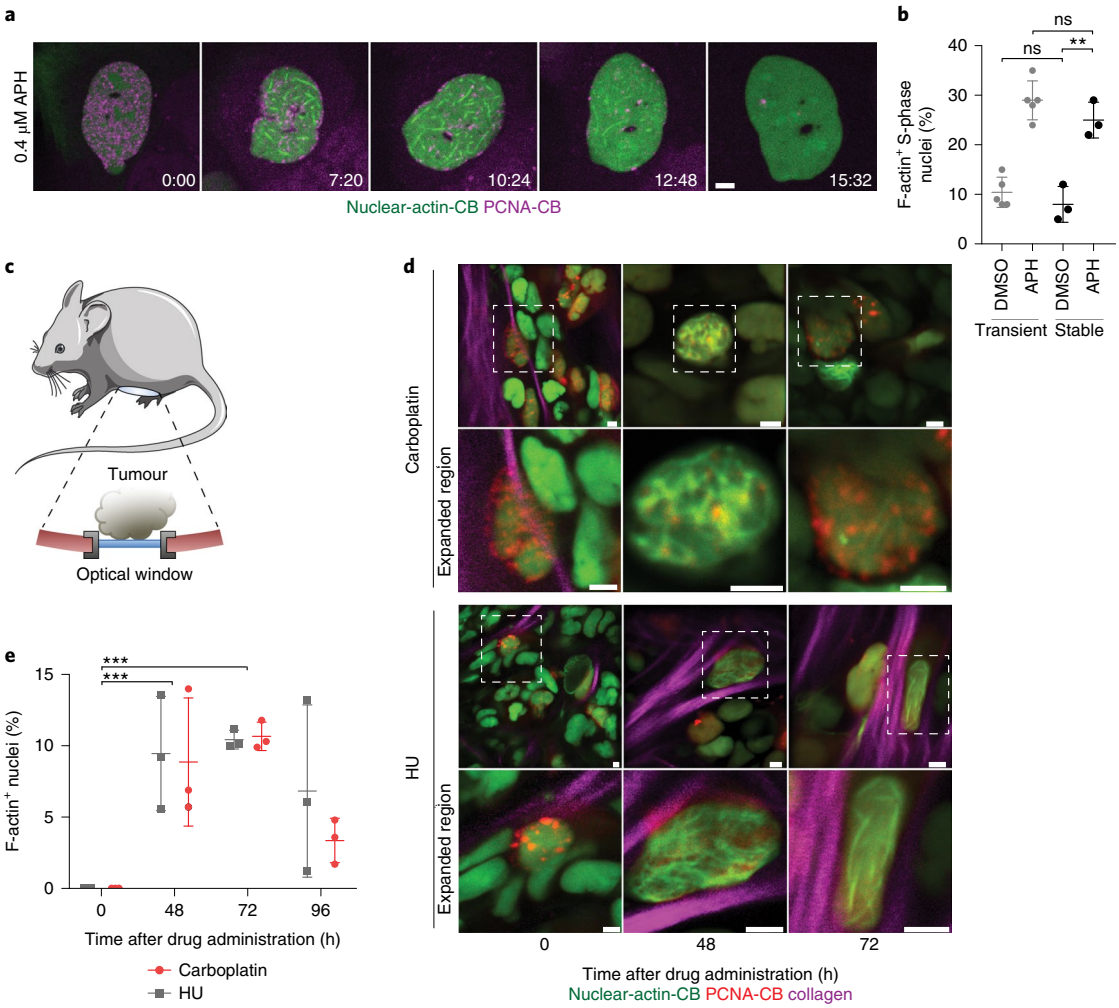


**Fig. 6 | Replication stress induces nuclear F-actin in vivo. a**, Still images from spinning-disk confocal live microscopy of APH-treated (0.4 μM) U-2OS cells stably expressing nuclear-actin-CB and PCNA-CB. Time is in hours:minutes relative to the first image of the series. Scale bar, 5 μm. **b**, Quantification of F-actin+ S-phase nuclei in U-2OS cells transiently or stably expressing nuclear-actin-CB and PCNA-CB and treated with DMSO or 0.4 μM APH. The data presented for the transient samples were pooled from Figs. 1e and 2f. Data are mean ± s.d. $n = 5$ (transient samples) and $n = 3$ (stable samples) biological replicates, scoring ≥36 nuclei per replicate. Statistical analysis was performed using two-sided Fisher's exact tests. **c**, Diagram of intravital microscopy through an optical window of human xenograft tumours in the inguinal fat pad of immunocompromised mice. Illustration was adapted from Servier Medical Art, licensed under the Creative Commons Attribution 3.0 Unported license. **d**, Example images from intravital microscopy of xenograft U-2OS tumours expressing nuclear-actin-CB and PCNA-CB before and after administration of 100 mg kg$^{-1}$ HU or 60 mg kg$^{-1}$ carboplatin by intraperitoneal injection. Collagen was visualized through second harmonic generation. Scale bars, 5 μm. **e**, Quantification of the percentage of F-actin+ nuclei from the experiments in **d** before and after drug administration. Data are mean ± s.e.m. $n = 3$ mice for each drug condition, scoring ≥51 nuclei per time point in each mouse. Statistical analysis was performed using unpaired two-tailed *t*-tests. For **b** and **e**; ns, not significant; $^{**}P < 0.01$, $^{***}P < 0.001$. Source data are available online.

contemporaneously with reversible replication stress before fork collapse. Nuclear actin polymerization was also regulated by ATR—the master regulator of the replication stress response. Functionally, nuclear F-actin mitigated replication-stress-induced nuclear deformation, promoted replication stress repair and suppressed replication-stress-induced chromosome and mitotic abnormalities. Finally, we confirmed that nuclear-specific F-actin activities promoted replication stress repair and altered the nuclear architecture.

These data indicate that nuclear F-actin functions in a systemic response to replication stress. The APH dose-dependent response indicates that a threshold of replication stress is required to promote polymerization of nuclear actin cables. A coordinated systemic response is consistent with the observed nuclear-wide F-actin networks. In this context we propose that F-actin provides isotropic mechanical forces that shape and stabilize the nucleus. This counteracts replication-stress-induced nuclear deformation and results in an increase in nuclear volume and sphericity. Persistent F-actin bundles maintained during replication stress suggest that nuclear actin forces are upheld until replication is complete or replication stress is resolved. We can only speculate how increased nuclear volume contributes to replication stress repair. Possibilities include providing space within the nucleus to promote DNA metabolism, and increasing the nuclear membrane area to provide a larger platform for lamina-associated processes, including chromatin remodelling and replication fork repair[49,50].

Increased PCNA-CB focus mobility during replication stress is consistent with chromatin movement facilitating repair activity[51]. WASP and ARP2/3 were identified to promote localized diffusive DSB mobility and homology-directed repair in G2-phase human cells[13]. However, G2-phase breaks did not impact the nuclear volume or sphericity, nor did they induce polymerization of

nuclear-wide actin networks[13]. Our data demonstrate that nuclear F-actin polymerization occurs after replication stress, before fork collapse. This suggests that distinct actin pathways function in human cells during the replication stress and G2-phase DSB responses. During replication stress, PCNA-CB focus mobility was primarily confined and punctuated with bursts of diffusive or directed movement. Localized diffusive mobility is consistent with local restart of stalled replication forks. Directed PCNA focus movement was less common. However, these types of motion are consistent with observations in *Drosophila* and yeast where DNA lesions mobilize to the nuclear periphery to promote specialized repair reactions[12,52,53]. We postulate that, in contrast to the limited and localized actin functions that occur with mammalian G2-phase homology-directed repair[13], the replication stress response capitalizes on the full extent of the ability of nuclear F-actin to alter the nuclear environment and promote repair through multiple processes dependent on the underlying lesion[3].

It was previously suggested that mTOR has a function in the replication stress response through undefined mechanisms[20]. We found that mTORC1 promotes nuclear F-actin polymerization in response to replication stress. ATR and IPMK were implicated in mTOR activation, although these kinases may act in parallel pathways regulating F-actin dynamics. mTORC1 specificity was surprising because actin cytoskeleton remodelling is primarily attributed to mTORC2 (refs. [54,55]), and TORC2 was implicated in promoting yeast survival against genomic damage[23,24,56]. Notwithstanding, we found that the mTORC1-binding partner IQGAP1 regulates nuclear F-actin, consistent with mTORC1 and IQGAP1 regulation of WASP and ARP2/3 (refs. [33,57]). It remains unclear whether mTORC1 activity in this pathway is nuclear and/or cytoplasmic. Furthermore, we found that LIM kinase maintains nuclear F-actin in replication-stressed cells in agreement with inhibition of cofilin-1-mediated F-actin disassembly[58]. Finally, we found that nuclear F-actin is polymerized in vivo after chemotherapeutic intervention. Cancer cells often rely on the replication stress response to cope with endogenous replication threats[59]. The contribution of nuclear F-actin in promoting cancer cell survival, how this is affected clinically with ATR or mTOR inhibitors, and the potential cancer-cell-specific vulnerabilities within this pathway are of interest.

## Online content

Any methods, additional references, Nature Research reporting summaries, source data, extended data, supplementary information, acknowledgements, peer review information; details of author contributions and competing interests; and statements of data and code availability are available at https://doi.org/10.1038/s41556-020-00605-6.

Received: 3 February 2020; Accepted: 26 October 2020;
Published online: 30 November 2020

## References

1. Zeman, M. K. & Cimprich, K. A. Causes and consequences of replication stress. *Nat. Cell Biol.* **16**, 2–9 (2014).
2. Saldivar, J. C., Cortez, D. & Cimprich, K. A. The essential kinase ATR: ensuring faithful duplication of a challenging genome. *Nat. Rev. Mol. Cell Biol.* **18**, 622–636 (2017).
3. Cortez, D. Replication-coupled DNA repair. *Mol. Cell* **74**, 866–876 (2019).
4. Lopes, M. et al. The DNA replication checkpoint response stabilizes stalled replication forks. *Nature* **412**, 557–561 (2001).
5. Kumar, A. et al. ATR mediates a checkpoint at the nuclear envelope in response to mechanical stress. *Cell* **158**, 633–646 (2014).
6. Svitkina, T. The actin cytoskeleton and actin-based motility. *Cold Spring Harb. Perspect. Biol.* **10**, a018267 (2018).
7. Moore, H. M. & Vartiainen, M. K. F-actin organizes the nucleus. *Nat. Cell Biol.* **19**, 1386–1388 (2017).
8. Baarlink, C., Wang, H. & Grosse, R. Nuclear actin network assembly by formins regulates the SRF coactivator MAL. *Science* **340**, 864–867 (2013).
9. Plessner, M., Melak, M., Chinchilla, P., Baarlink, C. & Grosse, R. Nuclear F-actin formation and reorganization upon cell spreading. *J. Biol. Chem.* **290**, 11209–11216 (2015).
10. Baarlink, C. et al. A transient pool of nuclear F-actin at mitotic exit controls chromatin organization. *Nat. Cell Biol.* **19**, 1389–1399 (2017).
11. Belin, B. J., Lee, T. & Mullins, R. D. DNA damage induces nuclear actin filament assembly by formin-2 and Spire-(1/2) that promotes efficient DNA repair. *eLife* **4**, e07735 (2015).
12. Caridi, C. P. et al. Nuclear F-actin and myosins drive relocalization of heterochromatic breaks. *Nature* **559**, 54–60 (2018).
13. Schrank, B. R. et al. Nuclear ARP2/3 drives DNA break clustering for homology-directed repair. *Nature* **559**, 61–66 (2018).
14. Imseng, S., Aylett, C. H. & Maier, T. Architecture and activation of phosphatidylinositol 3-kinase related kinases. *Curr. Opin. Struct. Biol.* **49**, 177–189 (2018).
15. Saxton, R. A. & Sabatini, D. M. mTOR signaling in growth, metabolism, and disease. *Cell* **169**, 361–371 (2017).
16. Mok, K. W., Chen, H., Lee, W. M. & Cheng, C. Y. rpS6 regulates blood-testis barrier dynamics through Arp3-mediated actin microfilament organization in rat sertoli cells. An in vitro study. *Endocrinology* **156**, 1900–1913 (2015).
17. Mok, K. W., Mruk, D. D. & Cheng, C. Y. rpS6 regulates blood-testis barrier dynamics through Akt-mediated effects on MMP-9. *J. Cell Sci.* **127**, 4870–4882 (2014).
18. Padrick, S. B., Doolittle, L. K., Brautigam, C. A., King, D. S. & Rosen, M. K. Arp2/3 complex is bound and activated by two WASP proteins. *Proc. Natl Acad. Sci. USA* **108**, E472–E479 (2011).
19. Parisis, N. et al. Initiation of DNA replication requires actin dynamics and formin activity. *EMBO J.* **36**, 3212–3231 (2017).
20. Lamm, N., Rogers, S. & Cesare, A. J. The mTOR pathway: implications for DNA replication. *Prog. Biophys. Mol. Biol.* **147**, 17–25 (2019).
21. Essers, J. et al. Nuclear dynamics of PCNA in DNA replication and repair. *Mol. Cell. Biol.* **25**, 9350–9359 (2005).
22. Petermann, E., Orta, M. L., Issaeva, N., Schultz, N. & Helleday, T. Hydroxyurea-stalled replication forks become progressively inactivated and require two different RAD51-mediated pathways for restart and repair. *Mol. Cell* **37**, 492–502 (2010).
23. Schonbrun, M. et al. TOR complex 2 controls gene silencing, telomere length maintenance, and survival under DNA-damaging conditions. *Mol. Cell. Biol.* **29**, 4584–4594 (2009).
24. Shimada, K. et al. TORC2 signaling pathway guarantees genome stability in the face of DNA strand breaks. *Mol. Cell* **51**, 829–839 (2013).
25. Matsuoka, S. et al. ATM and ATR substrate analysis reveals extensive protein networks responsive to DNA damage. *Science* **316**, 1160–1166 (2007).
26. Shen, C. et al. TOR signaling is a determinant of cell survival in response to DNA damage. *Mol. Cell. Biol.* **27**, 7007–7017 (2007).
27. Kim, S. et al. Amino acid signaling to mTOR mediated by inositol polyphosphate multikinase. *Cell Metab.* **13**, 215–221 (2011).
28. Wang, Y. H. et al. DNA damage causes rapid accumulation of phosphoinositides for ATR signaling. *Nat. Commun.* **8**, 2118 (2017).
29. Maiso, P. et al. Defining the role of TORC1/2 in multiple myeloma. *Blood* **118**, 6860–6870 (2011).
30. Latres, E. et al. Insulin-like growth factor-1 (IGF-1) inversely regulates atrophy-induced genes via the phosphatidylinositol 3-kinase/Akt/mammalian target of rapamycin (PI3K/Akt/mTOR) pathway. *J. Biol. Chem.* **280**, 2737–2744 (2005).
31. Tekletsadik, Y. K., Sonn, R. & Osman, M. A. A conserved role of IQGAP1 in regulating TOR complex 1. *J. Cell Sci.* **125**, 2041–2052 (2012).
32. Bashour, A. M., Fullerton, A. T., Hart, M. J. & Bloom, G. S. IQGAP1, a Rac- and Cdc42-binding protein, directly binds and cross-links microfilaments. The. *J. Cell Biol.* **137**, 1555–1566 (1997).
33. Le Clainche, C. et al. IQGAP1 stimulates actin assembly through the N-WASP-Arp2/3 pathway. *J. Biol. Chem.* **282**, 426–435 (2007).
34. Johnson, M. A., Sharma, M., Mok, M. T. & Henderson, B. R. Stimulation of in vivo nuclear transport dynamics of actin and its co-factors IQGAP1 and Rac1 in response to DNA replication stress. *Biochim. Biophys. acta* **1833**, 2334–2347 (2013).
35. Arber, S. et al. Regulation of actin dynamics through phosphorylation of cofilin by LIM-kinase. *Nature* **393**, 805–809 (1998).
36. Dopie, J., Skarp, K. P., Rajakyla, E. K., Tanhuanpaa, K. & Vartiainen, M. K. Active maintenance of nuclear actin by importin 9 supports transcription. *Proc. Natl Acad. Sci. USA* **109**, E544–E552 (2012).
37. Lossaint, G. et al. FANCD2 binds MCM proteins and controls replisome function upon activation of S phase checkpoint signaling. *Mol. Cell* **51**, 678–690 (2013).
38. Sfeir, A. et al. Mammalian telomeres resemble fragile sites and require TRF1 for efficient replication. *Cell* **138**, 90–103 (2009).
39. Titus, M. A. Myosin-driven intracellular transport. *Cold Spring Harb. Perspect. Biol.* **10**, a021972 (2018).

40. de Lanerolle, P. & Serebryannyy, L. Nuclear actin and myosins: life without filaments. *Nat. Cell Biol.* **13**, 1282–1288 (2011).
41. Higuchi, H. & Takemori, S. Butanedione monoxime suppresses contraction and ATPase activity of rabbit skeletal muscle. *J. Biochem.* **105**, 638–643 (1989).
42. Straight, A. F. et al. Dissecting temporal and spatial control of cytokinesis with a myosin II inhibitor. *Science* **299**, 1743–1747 (2003).
43. Burrell, R. A. et al. Replication stress links structural and numerical cancer chromosomal instability. *Nature* **494**, 492–496 (2013).
44. Kedrin, D. et al. Intravital imaging of metastatic behavior through a mammary imaging window. *Nat. Methods* **5**, 1019–1021 (2008).
45. Nobis, M. et al. A RhoA-FRET biosensor mouse for intravital imaging in normal tissue homeostasis and disease contexts. *Cell Rep.* **21**, 274–288 (2017).
46. Madaan, K., Kaushik, D. & Verma, T. Hydroxyurea: a key player in cancer chemotherapy. *Expert Rev. Anticancer Ther.* **12**, 19–29 (2012).
47. Wagner, J. M. & Karnitz, L. M. Cisplatin-induced DNA damage activates replication checkpoint signaling components that differentially affect tumor cell survival. *Mol. Pharmacol.* **76**, 208–214 (2009).
48. Masamsetti, V. P. et al. Replication stress induces mitotic death through parallel pathways regulated by WAPL and telomere deprotection. *Nat. Commun.* **10**, 4224 (2019).
49. Singh, M. et al. Lamin A/C depletion enhances DNA damage-induced stalled replication fork arrest. *Mol. Cell. Biol.* **33**, 1210–1222 (2013).
50. Guerreiro, I. & Kind, J. Spatial chromatin organization and gene regulation at the nuclear lamina. *Curr. Opin. Genet. Dev.* **55**, 19–25 (2019).
51. Seeber, A., Hauer, M. H. & Gasser, S. M. Chromosome dynamics in response to DNA damage. *Annu. Rev. Genet.* **52**, 295–319 (2018).
52. Chung, D. K. et al. Perinuclear tethers license telomeric DSBs for a broad kinesin- and NPC-dependent DNA repair process. *Nat. Commun.* **6**, 7742 (2015).
53. Freudenreich, C. H. & Su, X. A. Relocalization of DNA lesions to the nuclear pore complex. *FEMS Yeast Res.* **16**, fow095 (2016).
54. Jacinto, E. et al. Mammalian TOR complex 2 controls the actin cytoskeleton and is rapamycin insensitive. *Nat. Cell Biol.* **6**, 1122–1128 (2004).
55. Sarbassov, D. D. et al. Rictor, a novel binding partner of mTOR, defines a rapamycin-insensitive and raptor-independent pathway that regulates the cytoskeleton. *Curr. Biol.* **14**, 1296–1302 (2004).
56. Cohen, A., Kupiec, M. & Weisman, R. Gad8 protein is found in the nucleus where it Interacts with the Mlui cell cycle box-binding factor (MBF) transcriptional complex to regulate the response to DNA replication stress. *J. Biol. Chem.* **291**, 9371–9381 (2016).
57. Swiech, L. et al. CLIP-170 and IQGAP1 cooperatively regulate dendrite morphology. *J. Neurosci.* **31**, 4555–4568 (2011).
58. Maekawa, M. et al. Signaling from Rho to the actin cytoskeleton through protein kinases ROCK and LIM-kinase. *Science* **285**, 895–898 (1999).
59. Ubhi, T. & Brown, G. W. Exploiting DNA replication stress for cancer treatment. *Cancer Res.* **79**, 1730–1739 (2019).

## Methods

**Cell culture and treatments.** IMR90, IMR90$^{E6E7}$ and U-2OS cells were provided by J. Karlseder (Salk Institute), and HT1080 6TG cells were provided by E. Stanbridge (University of California, Irvine). Cell Bank Australia verified cell line identity using short-tandem-repeat profiling, and all cells were identified to be mycoplasma negative (MycoAlert, LT07-118, Lonza). Cultures were grown at 37 °C, 10% $CO_2$ and 3% $O_2$ in DMEM (Life Technologies) supplemented with 1% non-essential amino acids (Life Technologies), 1% Glutamax (Life Technologies) and 1% penicillin–streptomycin (Life Technologies). IMR90 and derivatives were supplemented with 10% fetal bovine serum (Life Technologies), and U-2OS and HT1080 6TG cultures with 10% bovine growth serum (HyClone). DMSO (Sigma-Aldrich), APH (Sigma-Aldrich), HU (Sigma-Aldrich), LatB (Cayman Chemical, 10010631), INK128 (Cayman Chemical, 11811), VE-822 (Selleckchem, S7102), insulin-like growth factor 1 (IGF1, Sigma-Aldrich, SRP4121), CK-666 (Sigma-Aldrich, SML0006), wiskostatin (Sigma-Aldrich, W2270), LIMKi 3 (Calbiochem, 435930), 2,3-butanedione monoxime (Sigma-Aldrich, B0753), blebbistatin (Sigma-Aldrich, B0560) and MyoVin-I (Calbiochem, 475984) were used in cell treatments.

**Phalloidin staining.** Cells were seeded on sterile glass coverslips, treated with APH or HU 24 h later, and then fixed 24 h thereafter. Cells were fixed for 1 min in cytoskeleton buffer (10 mM MES, 150 mM NaCl, 5 mM EGTA, 5 mM glucose and 5 mM $MgCl_2$, pH 6.1) plus 0.5% Triton X-100 and 0.25% glutaraldehyde (Sigma-Aldrich), and then for 15 min in cytoskeleton buffer plus 2% glutaraldehyde. Autofluorescence was quenched with fresh 1 mg ml$^{-1}$ sodium borohydride (Sigma-Aldrich) and cover slips incubated overnight at 4 °C with phalloidin-Atto 488 (Sigma-Aldrich, 49409). Slides were washed four times for 5 min in 1× PBS and incubated for 3 h at 37 °C with anti-lamin A/C antibodies. The samples were washed again in the same manner, and then incubated with Alexa Fluor 568-conjugated secondary antibodies for 1 h at 37 °C. Slides were washed as described above, dehydrated in a graded ethanol series (70%, 90% and 100% for 2 min in each solution) and mounted with Prolong Gold (Life Technologies). To avoid complication of extranuclear signals, imaging was limited to cells with a clearly resolvable nuclear interior. Antibodies were diluted in 1× PBS plus 5% fetal calf serum.

**Preparation of nuclear and cytoplasmic extracts.** When appropriate, cells were treated with APH for 8 h. Cultures were washed once with cold 1× PBS, scraped carefully and centrifuged at 800*g* for 10 min. The pellet was kept at −80 °C for 45 min, and then resuspended in buffer P1 (5 × 10$^6$ cells in 250 µl of 10 mM HEPES, 0.1 mM EGTA, 1 mM dithiothreitol (DTT), complete protease inhibitors (Roche)). Triton X-100 was added to 0.5%, the samples were vortexed for 10 s and the nuclei were sedimented at 10,000*g* for 10 min. The supernatant was retained as cytoplasmic extract. The nuclear pellet was then washed with buffer P1 before lysis in buffer P2 (5 × 10$^6$ cells in 100 µl of 20 mM HEPES, 25% glycerol, 400 mM NaCl, 1 mM EGTA, 1 mM DTT, complete protease inhibitors) for 90 min on a rotary shaker at 4 °C. Insoluble material was sedimented at 16,000*g* for 30 min and the remaining supernatant was retained as nuclear extract. Extract purity was determined by immunoblotting for α-tubulin and histone H2. In blots, a 5× greater volume of nuclear extract was loaded per lane as compared with cytoplasmic extracts.

**Pyrenyl–actin assembly assays.** The assay was adapted from previously described protocols[60]. Nuclear extracts were dialysed using a mini dialysis unit (Thermo Fisher Scientific) against XB buffer (10 mM HEPES, pH 7.7, 100 mM KCl, 2 mM $MgCl_2$, 0.1 mM $CaCl_2$, 5 mM EGTA, 1 mM DTT) for at least 3 h. Nuclear extracts were then incubated with pyrene-labelled actin (Cytoskeleton, BK003) and fluorescence was measured at 407 nm with excitation at 365 nm using an EnSpire Multimode Plate Reader and EnSpire Manager v.4.13.3005.1482 (PerkinElmer).

**Chromobody transfection and imaging.** The NLS–GFP–actin chromobody (Chromotek, acg-n, nuclear-actin-CB) and RFP–PCNA chromobody (Chromotek, ccr, PCNA-CB) were purchased with an material transfer agreement from Chromotek. Plasmids were transfected with Lipofectamine LTX (Thermo Fisher Scientific). For fixed imaging, cells were seeded on sterile cover slips and transfected 24 h later. Chemical inhibitors were added 48 h after transfection for 24 h. Samples were fixed in 3.7% formaldehyde/1× PBS for 10 min, permeabilized with 0.5% Triton X-100/1× PBS for 10 min at room temperature, dehydrated in a graded ethanol series (70%, 90% and 100%) and then mounted using Prolong Gold. For live-cell imaging, cells were seeded on a glass-bottom dish (3 cm; World Precision Instruments) and transfected 24 h later. Then, 48 h after transfection, cells were treated with the indicated compounds for 24 h. Culture medium was replaced with colourless DMEM (FluoroBrite DMEM, Life Technologies) supplemented as described above and, where applicable, was replenished with vehicle or experimental compounds. Imaging was performed at 37 °C, 10% $CO_2$ and 3% $O_2$ on a Zeiss Cell Observer SD spinning-disk confocal microscope using combined differential interference contrast and fluorescence imaging (a 561 nm laser, 7% excitation power, 1 × 1 binning, EM gain of 908; and a 488 nm laser, 6.5% excitation power, 1 × 1 binning, EM gain of 527) with appropriate filter sets and a ×63/1.3 NA oil-immersion objective. Ten images per *z* stack were captured in an image scaled to 47,504 px × 37,602 px at 10.05 µm × 7.96 µm using Zen Blue 2 v.2.0.14283.302 (ZEISS) and an Evolve Delta (Photometrics) camera every 90–200 s for up to 72 h. F-actin$^+$ nuclei represent the fraction of S-phase nuclei that were actin-fibre positive at least once during imaging.

**Transfection and imaging of actin overexpression plasmids.** pmCherry-C1 actin-3×NLS P2A mCherry (Addgene plasmid 58475; http://n2t.net/addgene:58475) and pmCherry-C1 R62D actin-3×NLS P2A mCherry (Addgene plasmid 58477; http://n2t.net/addgene:58477) were gifts from D. Mullins[11]. miRFP670-WT-actin-3×NLS (nuclear-WT-actin) and miRFP670-R62D-actin-3×NLS (nuclear-mutant-actin) were generated by replacing pmCherry-C1 with miRFP670 (ref. [61]) using in-Fusion cloning (Takara). Cells were transfected with nuclear-WT-actin or nuclear-mutant-actin with or without control or *IPO9* siRNAs using DharmaFECT 1 (Dharmacon). APH was added 24 h after transfection and imaging was performed 48–96 h after transfection.

**Telomere detection in S-phase cells.** Cells were grown on sterile glass cover slips, treated with the indicated compounds for 24 h and then pulse labelled with 100 µM EdU (Invitrogen, C10339) for 1 h before fixation in 3.7% formaldehyde/1× PBS for 15 min and permeabilization with 0.5% Triton X-100/1× PBS for 20 min. EdU was detected using the Click-iT EdU imaging kit (Invitrogen, C10339). Slides were incubated for 3 h at 37 °C with anti-TRF2 antibodies, washed four times for 5 min in 1× PBS and then incubated for 1 h at 37 °C with Alexa Fluor 488-conjugated secondary antibodies. Slides were then washed again in the same manner, dehydrated in a graded ethanol series (70%, 90% and 100%) and mounted with Prolong Gold. Antibodies were diluted in 1× PBS plus 5% fetal calf serum.

**FANCD2, RAD51 and IQGAP1 labelling.** 72 h after chromobody transfection and 24 h after APH addition, cells grown on sterile glass cover slips were fixed in 3.7% formaldehyde/1× PBS for 10 min, permeabilized with 0.5% Triton X-100/1× PBS and blocked with 5% bovine serum albumin (Sigma-Aldrich)/1× PBS. Samples were incubated with primary and secondary antibodies, washed, dehydrated and mounted as described above.

**Super-resolution imaging.** Super-resolution imaging was performed on a ZEISS LSM 880 AxioObserver confocal fluorescent microscope fitted with an Airyscan detector using a Plan-Apochromat ×63/1.4 NA M27 oil-immersion objective using ZEN Black 2.3 pro SP1 v.14.0.20.201 (ZEISS). Cells were imaged using 1.9% excitation power of 568 nm laser, 2% excitation power of 488 laser and 1.8% excitation power of 647 nm laser, with 1 × 1 binning for all laser conditions in combination with the appropriate filter sets. Ten or more *z* stacks were captured with frame scanning mode and unidirectional scanning. *z* stacks were Airyscan processed using batch mode in Zen software.

**siRNA transfection.** Non-targeting (control siRNA, D-001810-10), *ATR* (L-003202-10), *MTOR* (L-003008-10), *RPTOR* (L-004107-10), *RICTOR* (L-016984-10), *IQGAP1* (L-004694-10), *ACTR2* (L-012076-5), *ACTR3* (L-012077-5) and *IPO9* (L-016863-5) ON-TARGETplus siRNA pools (Dharmacon) and *IPMK* (D-006740-05) siGENOME siRNAs (Dharmacon) were transfected using Lipofectamine RNA imax (Thermo Fisher Scientific).

**Western blotting.** Preparation of whole-cell extracts and western blots was performed as described previously[62] and luminescence was visualized on an LAS 4000 Imager using Multi Gauge v.3.0 (Fujifilm). Source data are available online.

**Molecular combing assays.** Molecular combing assays were adapted from previously published protocols[63]. Cultures were sequentially pulse-labelled with 100 µM IdU (Sigma-Aldrich) then CldU (Sigma-Aldrich) for 30 min (DMSO-treated cells) or 3 h (APH-treated cells). APH (0.4 µM) was added 1 h before IdU addition and kept in the culture medium throughout IdU and CldU labelling. Genomic DNA was stretched onto glass slides at 2 kb µm$^{-1}$ using a molecular combing system (Genomic Vision). IdU and CldU stained using immunofluorescence were captured using a ZEISS AxioImager Z.2, using a ×63/1.4 NA oil-immersion objective, appropriate filter cubes, an Axiocam 506 monochromatic camera (ZEISS) and Zen Blue Pro v.2.3.69.01015 (ZEISS). Only replication forks with an origin of replication as well as with both IdU and CldU staining were scored, and replication rates were calculated on both the IdU and CldU tracks. Fork distance is the length between sister forks measured from the end of the CldU tracks and is approximately half the length of the entire replicon[64]. Replicon length scales with, and serves as readout of, interorigin distance[64]. IdU and CldU track lengths were converted to kilobase pairs with Zen software using the constant and sequence-independent stretching factor (1 µm = 2 kb).

Replication recovery rates were similarly measured using molecular combing, except the cells were pulse-labelled for 3 h with IdU in the presence of 0.1 µM APH to arrest replication forks. APH and IdU were washed out and CldU was added to the culture medium for 30 min. Where appropriate, LatB, INK128 or VE-822 was added with CldU. Replication recovery rates were determined on the basis of CldU track lengths using the constant 1 µm = 2 kb. For all molecular combing,

*n* describes the number of individual forks. For distance analysis, this is half of the data points, one for two forks moving away from the origin. For experiments using siRNAs with or without miRFP670-actin-3×NLS expression, cells were transfected 70 h before IdU addition.

**FUCCI live-cell imaging and analysis.** mVenus-hGeminin (1/110)/pCSII-EF and mCherry-hCdt1(30/120)/pCSII-EF were gifts from A. Miyawaki[65]. IMR90$^{E6E7}$ FUCCI cells were created, imaged and analysed as described previously[48]. LatB was added 2 h before imaging.

**Visualizing chromosome segregation errors.** Cells were grown on sterile glass coverslips and treated with LatB with or without APH for 24 h before 10 min fixation in 3.7% formaldehyde/1× PBS, permeabilization in 0.5% Triton X-100/1× PBS. Cells were then stained with 1 μg ml$^{-1}$ DAPI (Sigma-Aldrich), ethanol dehydrated and mounted with Prolong Gold. Samples were imaged using a ZEISS AxioImager Z.2 with a ×63/1.4 NA oil-immersion objective, appropriate filter cubes, an Axiocam 506 monochromatic camera and Zen 2.3 Pro v.2.3.69.01015. Images were scored by eye.

**Cytogenetic analysis.** Cells were treated with DMSO or LatB for 24 h, then 100 ng ml$^{-1}$ colcemid (Thermo Fisher Scientific) for 40–60 min. Cells were collected by trypsinization, treated with hypotonic solution (27 mM KCl, 65 mM tri-sodium citrate) at 37 °C for 30 min and fixed with multiple changes of methanol:acetic acid 3:1. Fixed cells were kept at −20 °C until analysis. For analysis of gaps, constriction or breaks, cytogenetic chromosome spreads were prepared and stained with DAPI. Images were captured using a ZEISS AxioImager Z.2 with a ×63/1.4 NA oil-immersion objective, appropriate filter cubes and a CoolCube1 camera using a Metasystems automated metaphase finding and image acquisition platform (Metasystems metafer 4 v.3.12.8). Images are presented in negative.

**Cell line generation for xenograft tumours.** Actin chromobody (VHH)–GFP–NLS and PCNA chromobody (VHH)–RFP regions were PCR amplified from their respective Chromotek constructs using actin VHH-GFP-NLS F: GGCGCCGGCCGGATCTAGTTATTAATAGTAATCAATTACG and R: CTGTGCTGGCGAATTTTACACCTTCCGCTTTTTCTTAGGCG; and PCNA VHH-RFP F: GGCGCCGGCCGGATCTAGTTATTAATAGTAATCAATTACG and R: TGTGCTGGCGAATTCTCAATTAAGTTTGTGCCCCAGTTTG. PCR products were cloned into BamHI- and EcoRI-linearized (NEB) pWZL using Infusion Cloning (Takara). Plasmids were transfected into Phoenix retrovector packaging cells using Lipofectamine 3000 (Invitrogen, L3000-015), and the medium was replaced 16 h after transfection. Medium from the transfected Phoenix cultures was collected 48 h after transfection, filtered and administered to U-2OS cells. Targeted U-2OS cells were selected with 100 μg ml$^{-1}$ hygromycin (Sigma/Merck) for 5 d, and sorted using a BD Influx cell sorter at the Westmead Institute for Medical Research. Cells were initially transduced with PCNA-CB and sorted for high RFP expression, then subsequently transduced with nuclear-actin-CB and sorted for RFP and GFP double-positive cells. For live imaging of the stable cell line in culture, sorted double-positive cells were plated onto a glass-bottom dish and treated with DMSO or 0.4 μM APH the next day. Cells were imaged 12 h after APH treatment for 48 h.

**Animal study ethics statement.** Animal experiments were conducted in accordance with the Garvan Institute of Medical Research Animal Ethics Committee (guidelines 19/13) and in compliance with the Australian code of practice for care and use of animals for scientific purposes.

**Implantation of optical imaging windows.** Mice were kept in standard housing at 21 ± 1 °C with an average humidity of 50%, in 12 h daylight cycles and fed ad libitum. Cage enrichment was undertaken by supplying the fully plastic individually ventilated cages with papier-mâché domes, feeding trays on the cage floor and soft tissue paper as nesting material. NOGIL2 mice (NOD.Cg-PrkdcscidIL2rgtm1Wjl/SzJAusb) were injected with $1 \times 10^7$ nuclear-actin-CB- and PCNA-CB-expressing U-2OS cells subcutaneously near to the inguinal mammary fat pad. After development of palpable tumours, mice were engrafted with titanium mammary imaging windows (Russell Symes & Company)[44,45,66,67]. In brief, mice were treated with 5 mg kg$^{-1}$ of the analgesic Carprofen (Rimdayl) in pH-neutral drinking water 24 h before and up to a minimum of 72 h after surgery. Mice also received subcutaneous injections of buprenorphine (0.075 mg kg$^{-1}$, Temgesic) immediately before and 6 h after surgery. The titanium window was prepared 24 h before surgery by gluing a 12 mm glass coverslip (Electron Microscopy Science) using cyanoacrylate to the groove on the outer rim of the titanium window. After anaesthetic induction at 4% isoflurane delivered using a vaporizer (VetFlo) supplemented with oxygen, mice were kept at a steady 1–2% maintenance anaesthesia for the duration of the surgery on a heated pad. The incision site was shaved and depilated (Nair) and disinfected using 0.5% chlorhexidine/70% ethanol. A straight incision was made into the skin above the developed subcutaneous tumour and, after blunt dissection of the skin surrounding the incision, a purse string suture (5–0 Merslik, Ethicon) was placed. The windows were then inserted and held in place by tightening the suture, which disappeared along with the skin into the groove of the window, and the suture was tied off. Mice recovered for a minimum of 72 h after surgery, and were actively foraging, feeding and grooming within minutes after being removed from the anaesthesia respirator. A minimum of 24 h before imaging, mice were weaned off the carprofen analgesic in the drinking water.

**Intravital imaging.** Mice were imaged under 1–2% isofluorane on a heated stage (Digital Pixel) before and after intraperitoneal injection of 60 mg kg$^{-1}$ carboplatin (Abcam) or 100 mg kg$^{-1}$ HU (Sigma-Aldrich). Multi-photon imaging was performed using a Leica DMI 6000 SP8 confocal microscope with a ×25/0.95 NA water-immersion objective on an inverted stage. The Ti:Sapphire femto-second laser (Coherent Chameleon Ultra II, Coherent) excitation source operating at 80 MHz was tuned to a pumping wavelength of 840 nm. The optical parametric oscillator (Chameleon Compact OPO, Coherent) was pumped with 80% of the Ti:Sapphire output and tuned to a wavelength of 1,100 nm. Reflected light detection - hybrid detectors were used with 435/40, 525/50 and 617/70 bandpass emission filters to detect the second harmonic generation of the collagen I, EGFP and mCherry, respectively. Images were acquired using Leica Application Suite X (v.3.5.5.19976) at a line rate of 1,400–1,800 Hz, 512 px × 512 px and at a total of 203 frames per image. Realignment of the data was performed using Galene (v.2.0.2)[68] using the warp realignment mode, 10 realignment points, a smoothing radius of 2 px and a realignment threshold of 0.4 applied for the second harmonic generation channel and 0.6 for the remaining two channels. Images were processed using used ImageJ/Fiji (v.2.1.0/1.53c).

**Volume and sphericity measurements.** Imaging data were imported into Imaris v.8.4.1 (Bitplane), where nuclei were segmented using the Surfaces function on the actin-NLS channel. Volume and sphericity were calculated using the Volume and Sphericity functions. For live imaging, surfaces were tracked over time and volume and sphericity were calculated for every time point.

**Nuclear localization of replication foci and telomeres.** Imaging data were imported into Imaris v.8.4.1, where nuclei were segmented as 'cells' using the Cell function on the actin-NLS channel. Telomeres or PCNA foci were segmented as 'vesicles' using the Cell function. The distance between foci and the nuclear periphery were calculated using the function 'Distance of vesicles to cell membrane'.

**Measurement of late S-phase PCNA chromobody focus speed and displacement.** Imaging data were imported into Imaris v.8.4.1. Nuclei were segmented as 'Surfaces' using the Surface function on the actin-NLS channel. Nuclei speed was calculated using the Speed function. Then, late S-phase nuclear-actin-CB foci were segmented using the Spots function and their speed was determined using the Speed function. We subtracted nucleus speed from the focus speed to correct for cell movement. The direction of movement was determined by calculating the distance of late S-phase nuclear-actin-CB foci from the nuclear periphery using the Cell function as described above, and then subtracting the distance in the last frame from the distance in the first frame for each focus. To ensure that focus movement was not influenced by nuclear or cell movement, analysis was limited to nuclei in which the mobility of a PCNA-CB focus relative to the nuclear periphery overlapped temporally with the confinement of other PCNA-CB foci relative to the nuclear periphery. A 10% change in distance to the periphery was tolerated for the reference focus.

**Image processing for MSD analysis.** Imaging data were imported into Imaris v.8.4.1, where nuclei were coarsely segmented using the Surfaces function on the actin-NLS channel. Cells migrate on the substrate during acquisition. To correct for this, we developed an image processing method such that the position of the foci could be quantified in the nucleus frame of reference and not the laboratory frame of reference (Supplementary Video 6). We termed this technique 'registration'. To register nuclei, positional and morphological data on the segmented nucleus were transferred into MATLAB (v.R2018b; MathWorks) using the XT module of Imaris, where the centre of mass and the angle of the long axis of the 3D ellipsoid fit of the surface were retrieved using custom MATLAB code. The algorithm then placed, using the XT module in Imaris, reference frames centred on the centre of mass of the nuclei and oriented in the direction of the ellipsoid long axis at every timepoint. Rotations were allowed in only the *xy* plane, due to the adherent nature of the studied cells. Combined, both the translational and rotational movements of the cells could be stabilized without the need for considering a subset of foci as immobile fiducial markers. The registration operation was completed within Imaris using the Align Image function without interpolation, allowing for rotations and retaining the same dataset size as before registration. Subsequently, in the registered dataset, replication foci could be readily tracked using the Spots function in Imaris and Autoregressive Motion tracking; the numerical positional data was exported for further motion/MSD analysis.

**Replication focus MSD analysis.** Displacement values for a given replication focus were extracted from its positional time-series data (its 'track'). Displacement values for a given time interval were extracted from all of the possible temporal points in

the track, that is, they were not constrained to start at time zero only. Time points in the track of a replication focus track where positions could not be ascertained were omitted from the MSD analysis. Time intervals used in the MSD analysis comprise all multiples of the temporal gap between timeframes (determined by sampling frequency) for the given experiment, up to a maximum value of 20% of the track with the longest duration in the given nucleus. To analyse MSD dynamics of all foci at a population level, displacement values for each given time interval were pooled from all of the focus tracks before taking the mean. MSD slopes represent the gradient of a linear regression model fitted to log–log-transformed MSD time interval data.

MSD analysis was performed over individual tracks using a sliding window to provide a time-series of MSD slopes. The window width of nine positional timeframes defined the sliding window, and the MSD slope was assigned to the centre (fifth) timeframe. MSD slopes were categorized into 'MSD regimes' on the basis of the following: confined motion (MSD slope < 0.8), diffusive (Brownian) motion (0.8 < MSD slope < 1.2), hyperdiffusive motion (MSD slope > 1.2) and sustained hyperdiffusive motion (MSD slope > 1.2 for five or more consecutive timeframes). Experimental conditions were contrasted by pooling instances of observed MSD regimes from all of the tracks in each condition. Statistical significance between conditions in Fig. 4d,i were calculated using the chi2_ contingency function of the Python 3.7.2 scipy.stats module, operating over the absolute number of time frames in which each MSD regime was observed under each condition.

**Antibodies.** The following primary antibodies were used: anti-BrdU (mouse monoclonal for IdU detection, BD Biosciences 347580, 1:5); anti-BrdU (rat monoclonal for CldU detection, Abcam, ab6326, 1:25); anti-TRF2 (Novus, NB110-57130, 1:250); anti-FANCD2 (Abcam, ab2187, 1:250); anti-lamin A/C (Sigma-Aldrich, L1293, 1:1,000); anti-α-tubulin (Abcam, ab18251, 1:5,000); anti-histone H2A (Abcam, ab18255, 1:2,000); anti-vinculin (Sigma-Aldrich, V9131, 1:5,000); anti-mTOR, anti-mTOR (phosphorylated Ser 2448), anti-P70S6 (phosphorylated Ser 371), anti-4E-BP1 (phosphorylated Thr 37/46) (mTOR substrates kit, Cell Signaling Technology, 9862, 1:1,000); anti-4E-BP1 (Cell Signaling Technology, 9644, 1:1,000); anti-P70S6 (Cell Signaling Technology, 2708, 1:1,000); anti-PKCα/β-II (phosphorylated Thr 638/641) (Cell Signaling Technology, 9375, 1:1,000); anti-Akt (phosphorylated Ser 473) (Cell Signaling Technology, 4060, 1:1,000); anti-IPMK (OriGene, TA308405, 1:1,000); anti-IQGAP1 (Cell Signaling Technology, 29016, 1:2,500 for western blot and 1:200 for immunofluorescence); anti-cofilin 1 (Cell Signaling Technology, 5175, 1:2,000); anti-cofilin1 (phosphorylated Ser 3) (Cell Signaling Technology, 3313, 1:1,000); anti-raptor (Cell Signaling Technology, 2280, 1:1,000); anti-rictor (Cell Signaling Technology, 2114, 1:1,000); anti-importin 9 (Invitrogen, PA1-41395, 1:1,000); anti-Arp2 (Cell Signaling Technology, 3128, 1:1,000); anti-Arp3 (Abcam, ab49671, 1:1,000); anti-CHK1 (Cell Signaling Technology, 2360, 1:1,000); anti-CHK1 (phosphorylated Ser 345) (Cell Signaling Technology, 2348, 1:1,000); anti-RAD51 (Merck, PC130, 1:200); anti-RPA32 (Cell Signaling Technology, 52448, 1:1,000); anti-RPA32 (phosphorylated Ser 8) (Cell Signaling Technology, 83745, 1:1,000).

The following secondary antibodies were used: goat anti-mouse Alexa Fluor 488 (Thermo Fisher Scientific, A28175, 1:25 for molecular combing and 1:1,000 for fixed nuclei staining); goat anti-rat Alexa Fluor 594 (Thermo Fisher Scientific, A-11007, 1:25); goat anti-rabbit Alexa Fluor 488 (Thermo Fisher Scientific, A11034, 1:1,000); goat anti-rabbit Alexa Fluor 568 (Thermo Fisher Scientific, A-11011, 1:750); goat anti-rabbit Alexa Fluor 647 (Thermo Fisher Scientific, A21245, 1:750); goat anti-rabbit HRP (Dako, P0448, 1:1,000 for anti-phosphorylated primary antibodies, otherwise 1:3,000), goat anti-mouse HRP (Dako, P0447, 1:1,000 for anti-phosphorylated primary antibodies, otherwise 1:3,000).

**Statistics and reproducibility.** Except for the MSD analysis described above, statistical analyses were performed using GraphPad Prism v.7.04. Tukey box plots extend from the 25th to the 75th percentile with the line representing the median. The top whisker represents data points ranging up to the 75th percentile + (1.5 × the interquartile range), or the largest value data point if no data points are outside this range. The bottom whisker represents data points ranging down to the 25th percentile – (1.5 × the interquartile range), or the smallest data point if no data points were outside this range. Data points outside these ranges are shown as individual points. Figure legends describe the error bars, statistical methods and *n* for all of the experiments. Representative data, whenever shown, are characteristic of similar results from at least two independent biological replicates. Figures were prepared using Adobe Photoshop and Illustrator.

**Reporting Summary.** Further information on research design is available in the Nature Research Reporting Summary linked to this article.

## Data availability

All data supporting the findings of this study are available from the corresponding author on reasonable request. Source data are provided with this paper.

## Code availability

Custom MATLAB code for performing nuclear registration with Imaris XT (Bitplane) is available at http://www.matebiro.com/software/nuclearactin. Custom Python code for generating the sliding window MSD analysis is available at GitHub (https://github.com/marknormanread/motility_analysis_lamm2020). Both codes are released under the GNU general public license (v.3).

## References


60. Kitzing, T. M. et al. Positive feedback between Dia1, LARG, and RhoA regulates cell morphology and invasion. *Genes Dev.* **21**, 1478–1483 (2007).
61. Shcherbakova, D. M. et al. Bright monomeric near-infrared fluorescent proteins as tags and biosensors for multiscale imaging. *Nat. Commun.* **7**, 12405 (2016).
62. Van, Ly,D. et al. Telomere loop dynamics in chromosome end protection. *Mol. Cell* **71**, 510–525 (2018).
63. Lamm, N. et al. Genomic instability in human pluripotent stem cells arises from replicative stress and chromosome condensation defects. *Cell Stem Cell* **18**, 253–261 (2016).
64. Maya-Mendoza, A., Petermann, E., Gillespie, D. A., Caldecott, K. W. & Jackson, D. A. Chk1 regulates the density of active replication origins during the vertebrate S phase. *EMBO J.* **26**, 2719–2731 (2007).
65. Sakaue-Sawano, A. et al. Visualizing spatiotemporal dynamics of multicellular cell-cycle progression. *Cell* **132**, 487–498 (2008).
66. Gligorijevic, B., Kedrin, D., Segall, J. E., Condeelis, J. & van Rheenen, J. Dendra2 photoswitching through the mammary imaging window. *J. Vis. Exp.* **28**, 1278 (2009).
67. Ritsma, L. et al. Surgical implantation of an abdominal imaging window for intravital microscopy. *Nat. Protoc.* **8**, 583–594 (2013).
68. Warren, S. C. et al. Removing physiological motion from intravital and clinical functional imaging data. *eLife* **7**, e35800 (2018).


## Acknowledgements


We thank S. Page and staff at the Australian Cancer Research Foundation Telomere Analysis Centre at the Children's Medical Research Institute for microscopy infrastructure; D. Croucher and V. Wickramshinghe for their feedback. M.B. acknowledges Bitplane for an Imaris Developer license. N.L. is supported by a Cancer Institute NSW early career fellowship and Kids Cancer Alliance grant, a Hebrew University Smorgon Foundation Fellowship, and bridging funds from University of Sydney. M.N.R. is supported by the University of Sydney Centre for Excellence in Advanced Food Enginomics. M.N. is supported by a fellowship from Cancer Institute NSW and grants from the St Vincent's Clinic Foundation and the Australian NHMRC. V.P.M. is supported by an Australian post-graduate award from the University of Sydney. P.T. is supported by a fellowship and grants from the Australian NHMRC and support from Len Ainsworth and Sutton group. M.B. is supported by funding from the European Molecular Biology Laboratory, Australia. A.J.C. is supported by grants from the Australian NHMRC (nos. 1053195, 1106241 and 1104461), the Cancer Council NSW (RG 15-12), the Cancer Institute NSW (11/FRL/5-02) and philanthropy from S. Brown (Sydney, Australia).


## Author contributions

N.L. and A.J.C. conceived the study. N.L., M.N., D.V.L., S.G.P. and V.P.M. performed experimentation. M.N. and P.T. provided intravital imaging. M.N.R. and M.B. developed analysis tools. N.L., M.N.R., M.N., M.B. and A.J.C. analysed the data. N.L., M.B. and A.J.C. created figures and wrote the manuscript.

## Competing interests

The authors declare no competing interests.

## Additional information


**Extended data** is available for this paper at https://doi.org/10.1038/s41556-020-00605-6.

**Supplementary information** is available for this paper at https://doi.org/10.1038/s41556-020-00605-6.



**Correspondence and requests for materials** should be addressed to A.J.C.

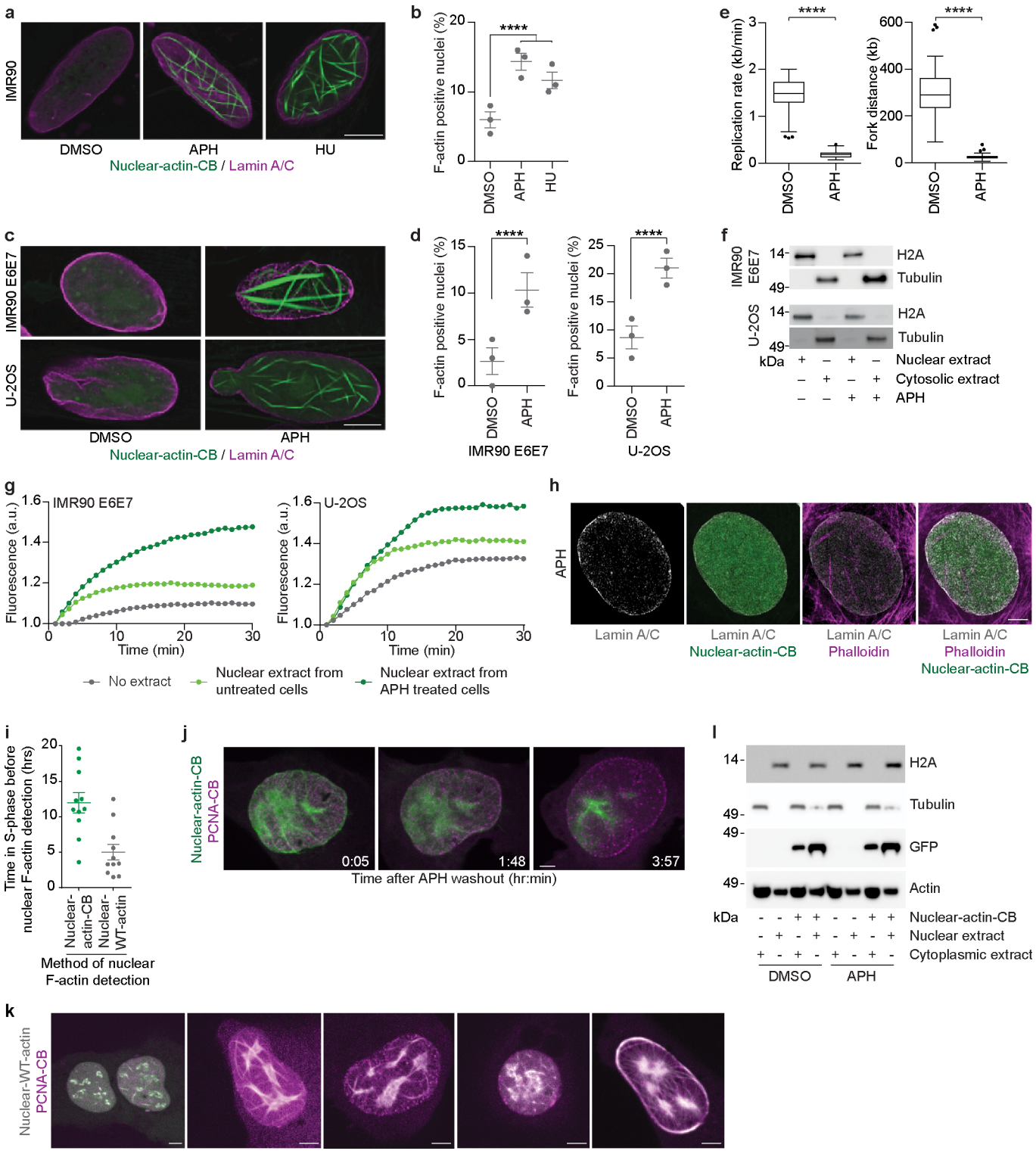


**Extended Data Fig. 1 | See next page for caption.**

**Extended Data Fig. 1 | Nuclear F-actin is induced and dissociated in S-phase with the introduction and removal of replication stress. a**-**d**, Nuclear-actin-CB expressing IMR90 (**a**, **b**), IMR90 E6E7 (**c**, **d**), and U-2OS (**c**, **d**) cultures treated with 0.4 μM APH or 500 μM HU for eight hours and stained for Lamin A/C (mean ± s.e.m, n = 3 biological replicates quantifying ≥ 58 nuclei per replicate, two-sided Fisher's exact test). Images are single Z-plane super-resolution micrographs through the nuclear volume. **e**, Replication rate and fork distance in IMR90 cells ± 0.4 μM APH assayed by molecular combing [replication rate n = 181 (DMSO) and 146 (APH), and fork distance n = 80 (DMSO) and 70 (APH), sampled from three biological replicates compiled into a Tukey box plot, unpaired two-tailed t-test]. **f**, Immunoblots of nuclear and cytosolic extracts from cultures treated ± 0.4 μM APH for eight hours. Volume of nuclear to cytoplasmic extract is 5:1. **g**, Normalised time course of pyrene-labelled actin assembly using the extracts from (**f**). **h**, Super-resolution single Z-plane images from a 0.4 μM APH treated U-2OS cell expressing nuclear-actin-CB fixed and stained for Lamin A/C and Phalloidin. **i**, Time in S-phase before nuclear F-actin was detected in 0.4 μM APH treated U-2OS cells expressing PCNA-CB and nuclear-WT-actin or nuclear-actin-CB (mean ± s.e.m., n = 11 cells per condition counted in 1 experiment). **j**, Live microscopy of nuclear-actin-CB and PCNA-CB transfected U-2OS cell treated with 0.4 μM APH for 24 hours before drug washout. **k**, Images of nuclear-actin-CB and nuclear-WT-actin expressing U-2OS cells with nucleolar actin. **l**, Western blots of nuclear and cytosolic extracts from U-2OS cultures ± nuclear-actin-CB expression. Nuclear to cytoplasmic extract volume is 5:1. For **f**, **g**, **j**, **k**, and **l**, data representative of three biological replicates are shown. For all panels: scale bar represents 5 μm, ****$p < 0.0001$. Source data and unprocessed blots are provided in Source Data Extended Data Fig. 1.

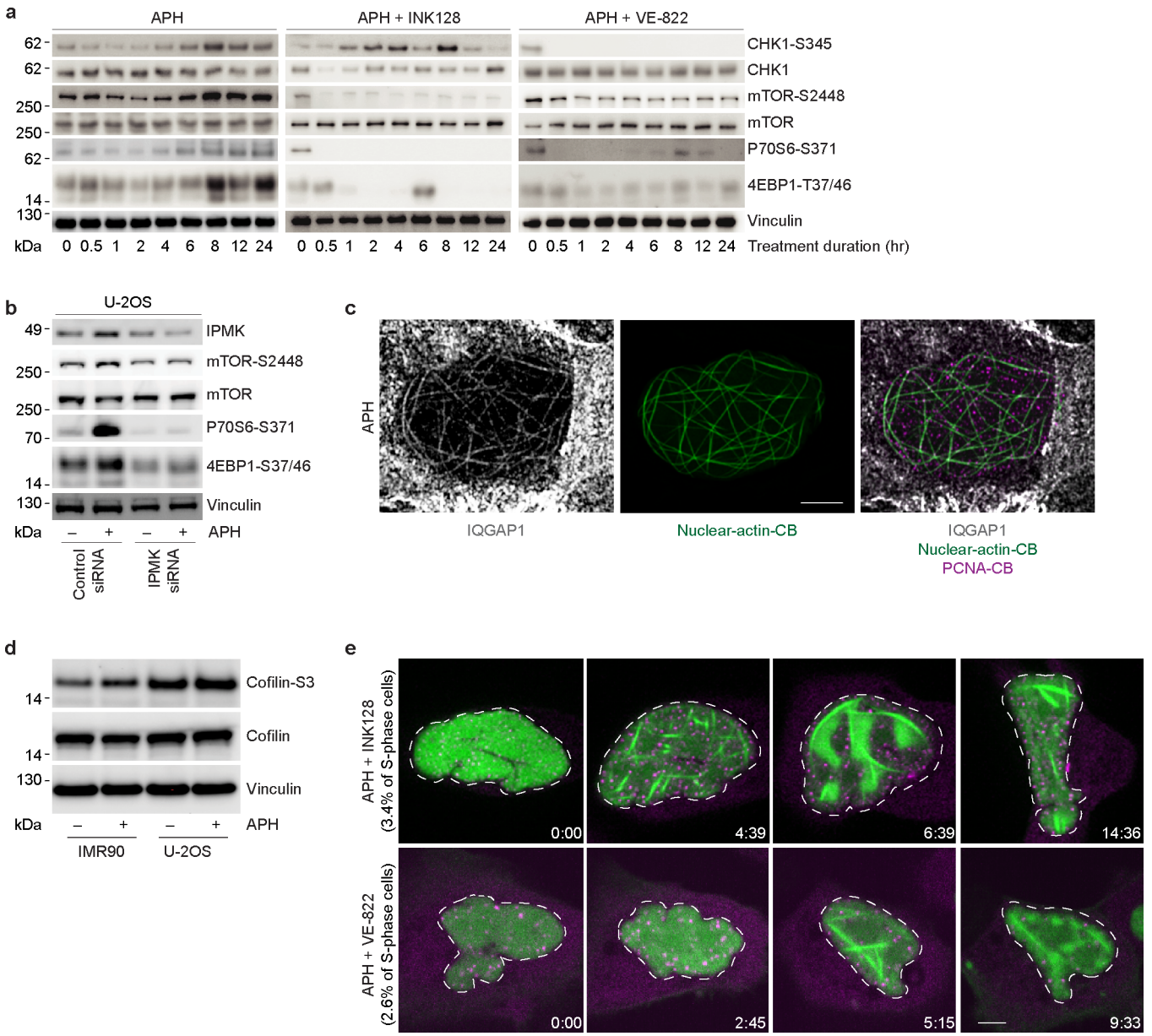


**Extended Data Fig. 2 | mTOR signalling, IQGAP1 localization to nuclear F-actin, and Cofilin1 phosphorylation occur with replication stress. a**, Western blots of whole cell extracts from IMR90 E6E7 cells treated with 0.4 μM APH ± 200 nM INK128 or 100 nM VE822 for the indicated duration. **b**, Western blots of whole cell extracts from siRNA transfected U-2OS cells treated with 0.4 μM APH for eight hours. Cells were siRNA transfected 48 hours prior to extraction. **c**, Single z-plane from super-resolution microscopy through the nucleus of a nuclear-actin-CB and PCNA-CB expressing U-2OS cell treated with 0.4 μM APH for 24 hours then fixed and stained for IQGAP1. **d**, Western blots of whole cell extracts from IMR90 or U-2OS cells treated ± 0.4 μM APH for 24 hours. **e**, Representative still images from live microscopy of nuclear-actin-CB and PCNA-CB expressing U-2OS cells where nuclear F-actin briefly assembled before losing structural integrity. Cells were treated with 0.4 μM APH + 200 nM INK128 or 100 nM VE822. Time is hr:min relative to the first image of the series. Cells displaying this phenotype were excluded from quantitative analyses shown elsewhere. All data in this figure are representative of at least two biological replicates. For all panels: scale bar represents 5 μm. Source data and unprocessed blots are provided in Source Data Extended Data Fig. 2.

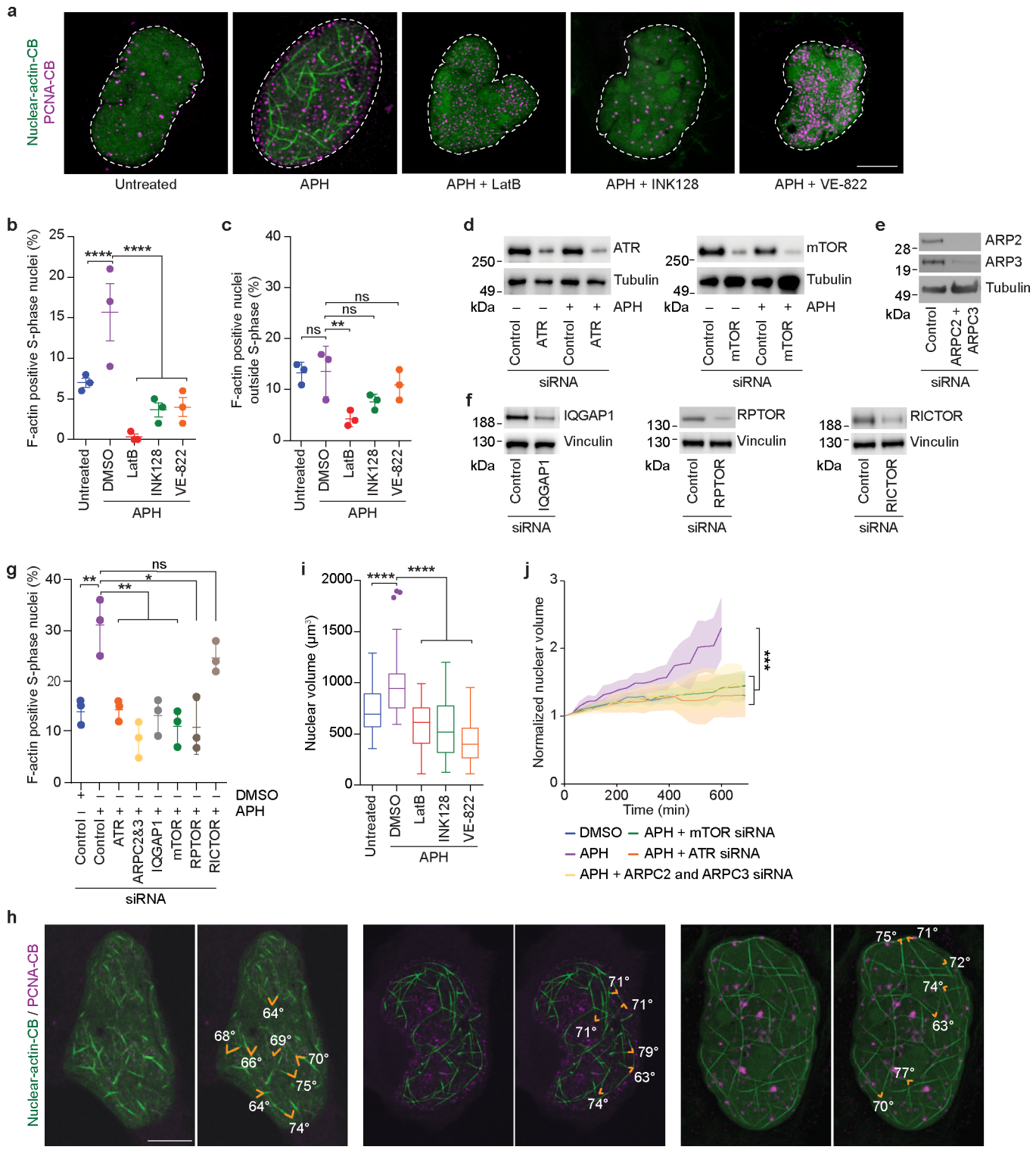


**Extended Data Fig. 3 | See next page for caption.**

**Extended Data Fig. 3 | Replication stress induces alteration of S-phase nuclear architecture through ATR, mTOR, and ARP2/3. a**, Single Z-plane super-resolution micrographs of fixed nuclear-actin-CB and PCNA-CB expressing IMR90 fibroblasts treated with 0.4 μM APH ± 200 nM LatB, 200 nM INK128, or 100 nM VE822 for 24 hours. **b**, **c**, Frequency of nuclear F-actin positive S-phase (**b**) and non-S-phase (**c**) nuclei from the experiment in (**a**) (mean ± s.e.m., n = 3 biological replicates scoring ≥ 51 S-phase and ≥ 32 non-S-phase nuclei per replicate, two-sided Fisher's exact test). **d**-**f**, Western blots of whole cell extracts from siRNA transfected U-2OS cells. Where applicable cells were treated with 0.4 μM APH for 8 hours. Data are representative of three biological replicates. **g**, Percentage of F-actin positive S-phase nuclei determined by live imaging of siRNA transfected U-2OS cells expressing nuclear-actin-CB and PCNA-CB. Cells were treated with vehicle or 0.4 μM APH (mean ± s.e.m., n = 3 biological replicates analyzing ≥ 40 cells per replicate, Fisher's exact test). **h**, Examples of 70° branched actin filaments in 0.4 μM APH treated U-2OS cells. **i**, S-phase nuclear volume from fixed nuclear-actin-CB and PCNA-CB expressing IMR90 cells [mean ± s.e.m., n = 125 (DMSO), 206 (APH), 125 (APH+LatB), 125 (APH+INK128), and 126 (APH+VE822) cells sampled from three biological replicates compiled into a Tukey box plot, unpaired two-tailed t-test]. **j**, Time course of normalised S-phase nuclear volume in nuclear-actin-CB and PCNA-CB expressing U-2OS cells treated with 0.4 μM APH and transfected with the indicated siRNAs [mean ± s.e.m., n = 34 (DMSO), 36 (APH), 15 (APH + mTOR siRNA), 16 (APH + ATR siRNA), and 15 (APH + ARP2/3 siRNA) nuclei sampled from two biological replicates, one-way ANOVA]. All panels: scale bar represents 5 μm, ns = not significant, *$p < 0.05$, ** $p < 0.01$, ****$p < 0.0001$. Source data and unprocessed blots are provided in Source Data Extended Data Fig. 3.

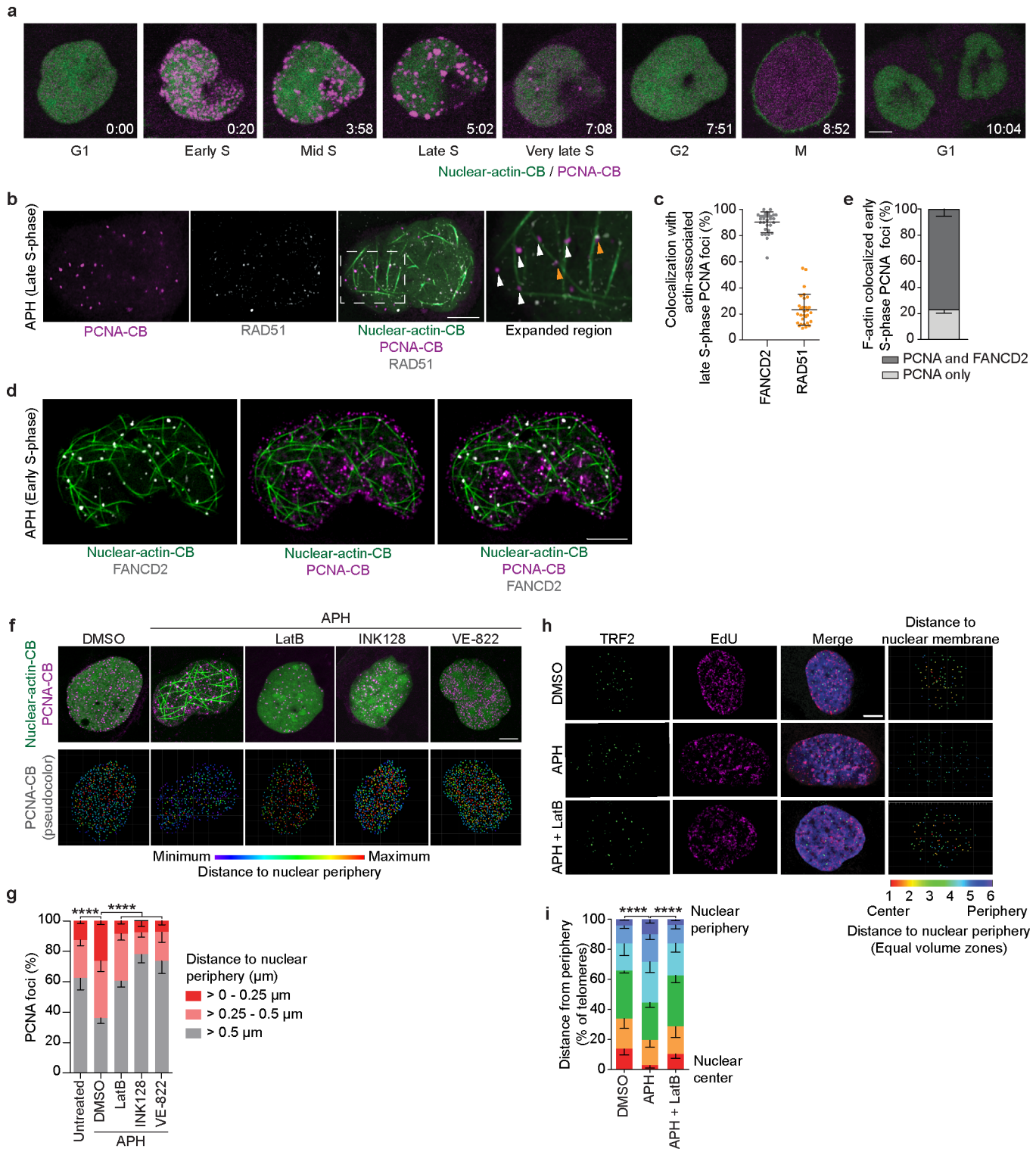


**Extended Data Fig. 4 | See next page for caption.**

**Extended Data Fig. 4 | Stressed replication foci localize to F-actin and the nuclear periphery. a**, PCNA-CB expressing U-2OS cell cycle (hr:min). **b**, Nuclear-actin-CB and PCNA-CB expressing late-S U-2OS cell treated with 0.4 μM APH for 24 hours and stained for RAD51. Arrows indicate RAD51-positive (orange) and -negative (white) actin-associated PCNA-CB foci. **c**, Co-localization between FANCD2 or RAD51 and late S-phase F-actin associated PCNA-CB foci (mean ± s.e.m., n = 30 cells pooled from three biological replicates). **d**, Early S-phase nuclear-actin-CB and PCNA-CB expressing U-2OS cell treated with 0.4 μM APH for 24 hours and stained for FANCD2. **e**, F-actin associated PCNA foci relative to FANCD2 in early and mid S-phase (mean ± s.e.m., n = 3 biological replicates scoring 21 cells total). **f**, Top: Super-resolution microscopy of single Z-planes from 3D images of nuclear-actin-CB and PCNA-CB expressing IMR90 cells treated with 0.4 μM APH ± 200 nM LatB, 200 nM INK128, or 100 nM VE822 for 24 hours. Bottom: PCNA-CB foci from the above 3D images collapsed into 2D and colour-coded for nuclear peripheral distance. **g**, Quantitation of (**f**) [mean ± s.e.m., n = 1684 (DMSO), 2155 (APH), 1695 (APH+LatB), 2001 (APH+INK128), and 2015 (APH+VE822) foci sampled from ≥ 12 nuclei across three biological replicates, Chi square test]. **h**, Left panels: super-resolution microscopy of single Z-planes from 3D images of U-2OS cells treated with 0.4 μM APH ± 200 nM LatB, labelled with EdU and stained for TRF2. Telomeres were assigned to one of six equal volume zones from nuclear centre to periphery. Right: Telomeres collapsed into 2D and colour-coded for nuclear volumetric zone. **i**, Quantitation of (**h**) [mean ± s.e.m., n = 2099 (DMSO), 2096 (APH), 3001 (APH+LatB) telomeres from ≥ 29 nuclei across three biological replicates, Chi square test]. All panels: Scale bar represents 5 μm, ****$p < 0.0001$. Source data provided in Source Data Extended Data Fig. 4.

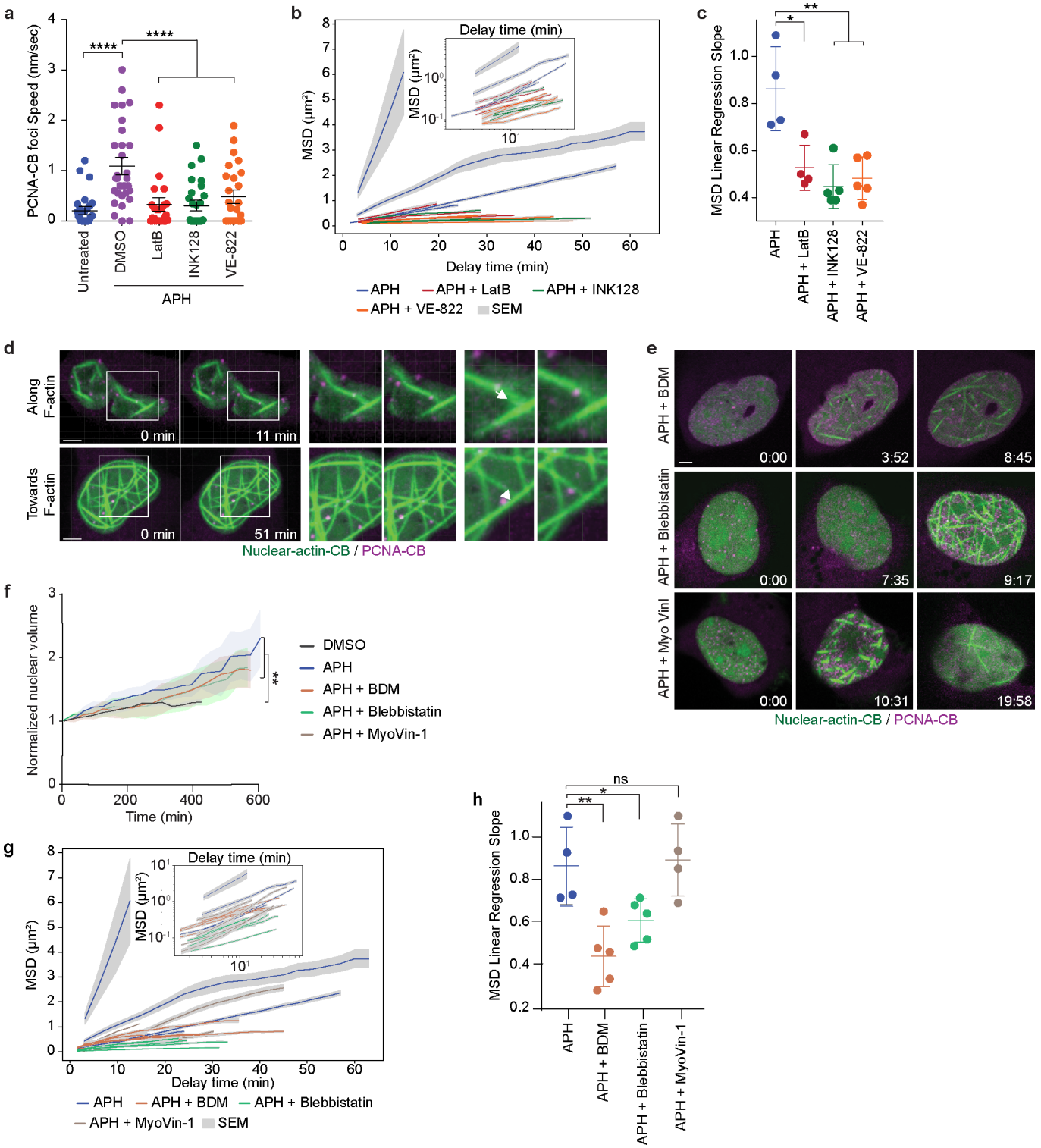


**Extended Data Fig. 5 | See next page for caption.**

**Extended Data Fig. 5 | ATR, mTOR and F-actin promote late replication foci mobility including movement along nuclear F-actin.** All data were collected from U-2OS cells expressing nuclear-actin-CB and PCNA-CB treated with or without DMSO, 0.4 μM APH, 200 nM LatB, 200 nM INK128, 100 nM VE-822, 10 mM BDM, 50 μM Blebbistatin, or 100 μM MyoVin-I. **a**, Average speed of late S-phase PCNA-CB foci [mean ± s.e.m., n = 30 (DMSO and APH), 26 (APH+LatB), 29 (APH+INK128), and 26 (APH+VE822) foci sampled from ≥ 7 nuclei compiled into a dot plot, unpaired two-tailed t-test]. **b**, **c**, Mean Squared Displacement (MSD) of replication foci trajectories. The lines in (**b**) represent individuals cells, with the inset showing MSD curves in log-log space used to calculate linear regression slopes for each nucleus, (**c**) are the linear regression slope values from (**b**) [mean ± s.d., n = 4 (APH and APH+LatB) and 5 (APH+INK128 and APH+VE822) nuclei, two-tailed unpaired t-test]. **d**, Examples from live-imaging of diffusive late PCNA-CB foci movement along or towards nuclear F-actin. Expanded regions are shown on the right. Arrows depict PCNA-CB foci movement. **e**, Still images from live imaging of cells treated as indicated. Time is hr:min relative to the first image. **f**, Quantitation of S-phase nuclear volume in the experiment in (**e**) [mean ± s.e.m, n = 34 (DMSO), 36 (APH), 18 (APH+BDM), 19 (APH+Blebbistatin), and 18 (APH+MyoVin-I) nuclei sampled from two biological replicates, one-way ANOVA]. **g**, **h**, MSD analysis of replication foci trajectories in cells treated as in (**f**) and displayed as in (**b**, **c**) (mean ± s.e.m., n = 4 (APH and APH+Myo-VinI) and 5 (APH+BDM and APH+Blebbistatin) nuclei, unpaired two-tailed t-test). For all panels: Scale bar represents 5 μm, ns = not significant, *$p < 0.05$, ** $p < 0.01$, ****$p < 0.0001$. Source data are provided in Source Data Extended Data Fig. 5.

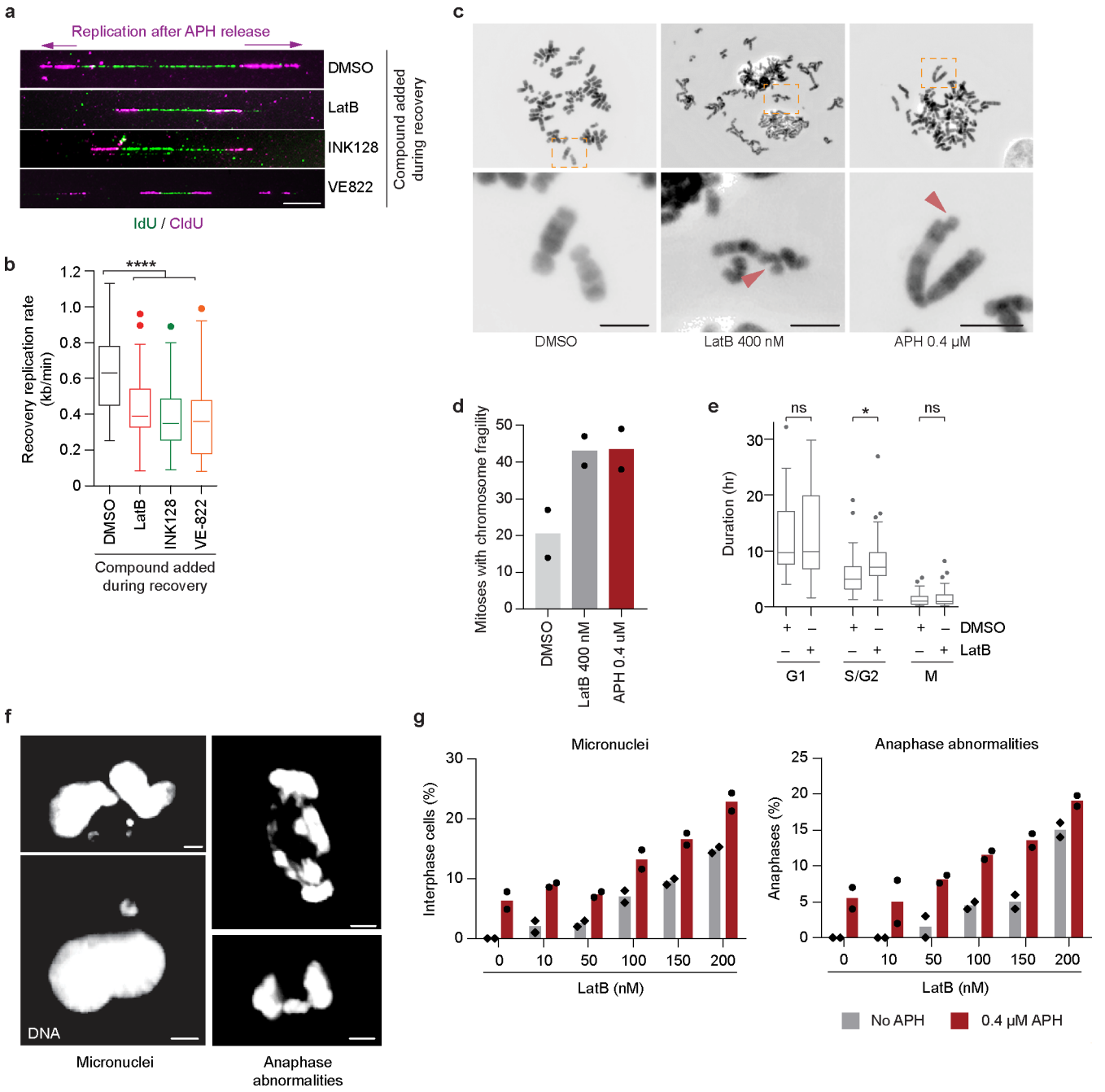


**Extended Data Fig. 6 | Inhibiting actin polymerization induces cellular and molecular outcomes consistent with unrepaired replication stress.** **a**, Molecular combing assays to measure recovery replication rate in IMR90 E6E7 cells. Cells were treated with 0.1 µM APH and IdU for three hours, before washout and labelling with CldU as shown in Fig. 5a. Following APH washout cells were treated with or without 200 nM LatB, 200 nM INK128, 100 nM VE-822. Scale bar represents 10 µm. **b**, Quantitation of the experiment shown in (**a**) [mean ± s.e.m., n = 142 (DMSO), 132 (LatB), 138 (INK128), and 138 (VE822) forks sampled from two biological replicates compiled into a Tukey box plot, two-tailed Student's t-test]. **c**, Cytogenetic chromosome preparations from U-2OS cells treated with LatB or APH for 24 hours before sample collection. Expanded images are shown below with examples of chromosome fragility indicated with red arrows. Scale bar represents 7.5 µm. **d**, Quantitation of the experiment depicted in (**c**) (n = 2 biological replicates, quantifying 78 mitoses per condition). **e**, Cell cycle phase duration from IMR90 E6E7-FUCCI cells treated with 200 nM [mean ± s.e.m., G1: n = 47 (DMSO and LatB), S/G2: n = 42 (DMSO) and 49 (LatB), M: n = 56 (DMSO) and 48 (LatB) cells sampled from three biological replicates and compiled into a Tukey box plot, unpaired two-tailed t-test). **f**, Micronuclei (left panels) and anaphase abnormalities (right panels) in IMR90 E6E7 cells following treatment with LatB. Scale bar represents 5 µm. **g**, Frequency of micronuclei and anaphase abnormalities in IMR90 E6E7 cells following treatment with escalating dosages of LatB (n = 2 biological replicates scoring ≥ 65 cells per replicate) For **d**, **g**, replicate means are shown as dot points, bar represents the overall mean. For all panels, ns = not significant, *p < 0.05, ****p < 0.0001. Source data are provided in Source Data Extended Data Fig. 6.

nature research

Corresponding author(s): Cesare, Anthony J.

Last updated by author(s): Oct 14, 2020

# Reporting Summary

Nature Research wishes to improve the reproducibility of the work that we publish. This form provides structure for consistency and transparency in reporting. For further information on Nature Research policies, see our Editorial Policies and the Editorial Policy Checklist.

## Statistics

For all statistical analyses, confirm that the following items are present in the figure legend, table legend, main text, or Methods section.

| n/a | Confirmed | |
|---|---|---|
| ☐ | ☒ | The exact sample size (*n*) for each experimental group/condition, given as a discrete number and unit of measurement |
| ☐ | ☒ | A statement on whether measurements were taken from distinct samples or whether the same sample was measured repeatedly |
| ☐ | ☒ | The statistical test(s) used AND whether they are one- or two-sided<br>*Only common tests should be described solely by name; describe more complex techniques in the Methods section.* |
| ☒ | ☐ | A description of all covariates tested |
| ☒ | ☐ | A description of any assumptions or corrections, such as tests of normality and adjustment for multiple comparisons |
| ☐ | ☒ | A full description of the statistical parameters including central tendency (e.g. means) or other basic estimates (e.g. regression coefficient) AND variation (e.g. standard deviation) or associated estimates of uncertainty (e.g. confidence intervals) |
| ☐ | ☒ | For null hypothesis testing, the test statistic (e.g. *F*, *t*, *r*) with confidence intervals, effect sizes, degrees of freedom and *P* value noted<br>*Give P values as exact values whenever suitable.* |
| ☒ | ☐ | For Bayesian analysis, information on the choice of priors and Markov chain Monte Carlo settings |
| ☒ | ☐ | For hierarchical and complex designs, identification of the appropriate level for tests and full reporting of outcomes |
| ☒ | ☐ | Estimates of effect sizes (e.g. Cohen's *d*, Pearson's *r*), indicating how they were calculated |

*Our web collection on statistics for biologists contains articles on many of the points above.*

## Software and code

Policy information about availability of computer code

| | |
|---|---|
| Data collection | ZEISS Zen Black 2.3 pro SP1 v 14.0.20.201<br>ZEISS Zen Blue 2.3 pro v2.3.69.01015 and Zen Blue 2 v2.0.14283.302<br>Metasystems Metafer 4 v3.12.8<br>Fuji film Multigauge v3.0<br>Enspire Manager v 4.13.3005.1482<br>Leica Application Suite X v3.5.5.19976<br>Galen v2.0.2 |
| Data analysis | Imaris 8.4.1<br>GraphPad Prism 7.04<br>MatLab R2018b<br>ImageJ/Fiji (v2.1.0/1.53c)<br>Python 3.7.2<br>Adobe Photoshop and Illustrator CC 2018 (Figure preparation) |

For manuscripts utilizing custom algorithms or software that are central to the research but not yet described in published literature, software must be made available to editors and reviewers. We strongly encourage code deposition in a community repository (e.g. GitHub). See the Nature Research guidelines for submitting code & software for further information.

## Data

Policy information about availability of data

All manuscripts must include a data availability statement. This statement should provide the following information, where applicable:

- Accession codes, unique identifiers, or web links for publicly available datasets
- A list of figures that have associated raw data
- A description of any restrictions on data availability

The manuscript contains the following data availability statement:

All data are stored at the Children's Medical Research Institute, the Garvan Institute of Medical Research, or the University of New South Wales. Source data are provided for Figures 1-6 and Extended Data Figures 1-6. All other data supporting the findings of this study are available from the corresponding author upon reasonable request. Requests for materials should also be addressed to the corresponding author.

# Field-specific reporting

Please select the one below that is the best fit for your research. If you are not sure, read the appropriate sections before making your selection.

☒ Life sciences ☐ Behavioural & social sciences ☐ Ecological, evolutionary & environmental sciences

For a reference copy of the document with all sections, see nature.com/documents/nr-reporting-summary-flat.pdf

# Life sciences study design

All studies must disclose on these points even when the disclosure is negative.

| | |
|---|---|
| Sample size | We did not compute statistical analyses to predetermine sample sizes prior to performing experiments. Sample sizes are consistent with previously published studies of a similar nature [Caridi et al. Nature 559, 54-60 (2018); Schrank et al. Nature 559, 61-66 (2018); Masamsetti et al. Nature communications 10, 4224 (2019); Lamm, N. et al. Cell stem cell 18, 253-261 (2016)]. |
| Data exclusions | No data were excluded. |
| Replication | All experiments were repeated in multiple biological replicates and in multiple cell lines whenever possible. The number of replicates is indicated in the figure legends and discussed in the statistics and reproducibility section of the methods. |
| Randomization | Cell culture experiments are not subjected to randomization. For intravital imaging of xenograft tumours, once mice reached a palpable tumour size and were implanted with optical windows, animals were randomly assigned to a treatment group. |
| Blinding | Investigators were blinded throughout data aqusition and analysis of molecular combing assays. Measurements of mean squared displacement, nuclear volume and sphericity, PCNA-CB and telomere nuclear localization, PCNA-CB foci speed and displacement, and pyrene actin assembly were not blinded but instead acquired and/or analyzed using automated software. Western blots are not subjected to blinding. |

# Reporting for specific materials, systems and methods

We require information from authors about some types of materials, experimental systems and methods used in many studies. Here, indicate whether each material, system or method listed is relevant to your study. If you are not sure if a list item applies to your research, read the appropriate section before selecting a response.

### Materials & experimental systems

| n/a | Involved in the study |
|---|---|
| ☐ | ☒ Antibodies |
| ☐ | ☒ Eukaryotic cell lines |
| ☒ | ☐ Palaeontology and archaeology |
| ☐ | ☒ Animals and other organisms |
| ☒ | ☐ Human research participants |
| ☒ | ☐ Clinical data |
| ☒ | ☐ Dual use research of concern |

### Methods

| n/a | Involved in the study |
|---|---|
| ☒ | ☐ ChIP-seq |
| ☒ | ☐ Flow cytometry |
| ☒ | ☐ MRI-based neuroimaging |

## Antibodies

| | |
|---|---|
| Antibodies used | Primary antibodies: BrdU (mouse monoclonal for IdU detection, BD Biosciences 347580); BrdU (rat monoclonal for CldU detection, abcam, ab6326); TRF2 (Novus, NB110-57130); FANCD2 (abcam, ab2187); Lamin A/C (Sigma-Aldrich, L1293); alpha tubulin (abcam, ab18251); H2A (abcam, ab18255); vinculin (Sigma-Aldrich, V9131); mTOR, mTOR-ser2448, P70S6-ser371, 4E-BP1-thr37/46 (mTOR substrates kit, Cell Signaling Technology, 9862); 4E-BP1 (Cell Signaling Technology, 9644); P70S6 (Cell Signaling Technology, 2708); |

PKCα/β II-Thr638/641 (Cell Signaling Technology, 9375); Akt-ser473 (Cell Signaling Technology, 4060); IPMK (OriGene, TA308405); IQGAP1 (Cell Signaling Technology, 29016); Cofilin1 (Cell Signaling Technology, 5175); Cofilin1-ser3 (Cell Signaling Technology, 3313); Raptor (Cell Signaling Technology, 2280); Rictor (Cell Signaling Technology, 2114); Importin 9 (Invitrogen, PA1-41395); Arp2 (Cell Signaling Technology, 3128); Arp3 (abcam, ab49671); CHK1 (Cell Signaling Technology, 2360); CHK1-ser345 (Cell Signaling Technology, 2348); RAD51 (Merck, PC130); RPA32 (Cell Signaling Technology, 52448); RPA32-ser8 (Cell Signaling Technology, 83745).

Secondary antibodies: goat anti-mouse Alexa Fluor 488 (ThermoFisher, A28175); goat anti-rat Alexa Fluor 594 (ThermoFisher, A-11007); goat anti-rabbit Alexa Fluor 488 (ThermoFisher, A11034); goat anti-rabbit Alexa Fluor 568 (ThermoFisher, A-11011); goat anti-rabbit Alexa Fluor 647 (ThermoFisher, A21245); goat anti-rabbit HRP (Dako, P0448); goat anti-mouse HRP (Dako, P0447).

Validation

Antibodies validated in this manuscript using siRNA depletion: mTOR (mTOR substrates kit, Cell Signaling Technology, 9862); IPMK (OriGene, TA308405); IQGAP1 (Cell Signaling Technology, 29016); Raptor (Cell Signaling Technology, 2280); Rictor (Cell Signaling Technology, 2114); Importin 9 (Invitrogen, PA1-41395); Arp2 (Cell Signaling Technology, 3128); Arp3 (abcam, ab49671);

Antibodies validated in the Cesare laboratory using siRNA depletion, data presented elsewhere or unpublished: TRF2 [Novus, NB110-57130; Van Ly et al. (2018) Molecular cell 71, 510-525]; RAD51 (Merck, PC130, R. Szmyd unpublished data); Cofilin1 (Cell Signaling Technology, 5175, N. Lamm unpublished data); Cofilin1-ser3 (Cell Signaling Technology, 3313, N. Lamm unpublished data);

Phospho-specific antibodies validated in this manuscript using selective chemical inhibitors: mTOR-ser2448, P70S6-ser371, 4E-BP1-thr37/46 (mTOR substrates kit, Cell Signaling Technology, 9862, 1:1000); CHK1-ser345 (Cell Signaling Technology, 2348)

Antibodies validated in this paper through other methods: Lamin A/C (Sigma-Aldrich, L1293) validated by immunofluorescence and localization to the nuclear periphery. BrdU (mouse monoclonal for IdU detection, BD Biosciences 347580) and BrdU (rat monoclonal for CldU detection, abcam, ab6326) were validated by immunoflourcence of direct incorporation into DNA in molecular combing assays. These are the gold standard antibodies for molecular combing (for example: Lamm, N. et al. (2016) Cell stem cell 18, 253-261).

Antibodies validated elsewhere
alpha tubulin (abcam, ab18251) is a commonly used loading control that stains a band of the appropriate molecular weight and labels microtubules when used with immunofluorescence. It is validated for use in western blots by the distributor. https://www.abcam.com/alpha-tubulin-antibody-microtubule-marker-ab18251.html

H2A (abcam, ab18255) is a commonly used ChIP grade antibody that pulls down nucleosomes, labels chromatin immunofluorescence and recognizes a protein of the correct molecular weight. It is validated for western blots by the distributor. https://www.abcam.com/histone-h2a-antibody-chip-grade-ab18255

Vinculin (Sigma-Aldrich, V9131) is a commonly used loading control, validated by miR depletion by the manufacturer, https://www.sigmaaldrich.com/catalog/product/sigma/v9131.

FANCD2 (abcam, ab2187) was validated by siRNA depletion in Howard et al. (2015) PLoS Genetics, 11:e1004943

P70S6 (Cell Signaling Technology, 2708) was validated by siRNA deletion in Wang et al. (2017) Heliyon, e00378.

4E-BP1 (Cell Signaling Technology, 9644) was validated by siRNA in Woodcock et al. (2019) Nature Communications, doi.org/10.1038/s41467-018-07858-8

Akt-ser473 (Cell Signaling Technology, 4060) was validated using selective chemical inhibitors by the manufacturer, https://www.cellsignal.com/products/primary-antibodies/phospho-akt-ser473-d9e-xp-rabbit-mab/4060?Ntk=Products&Ntt=4060. .

CHK1 (Cell Signaling Technology, 2360) was validated by molecular weight shift with tagging of exogenous allele in Yu et al (2020). J Hematol Oncol., 13: 40.

PKCα/β II-Thr638/641 (Cell Signaling Technology, 9375) was validated through stimulation by Thapsigargin in Taverner et al (2019). Mol Ther Oncolytics, 15:117-130.

RPA32 (Cell Signaling Technology, 52448) was validated through a band shift after UV irradiation by the manufacter https://en.cellsignal.jp/products/primary-antibodies/rpa32-rpa2-antibody/52448.

RPA32-ser8 (Cell Signaling Technology, 83745) was validated by inducation following UV induced damage by the manufacturer. https://en.cellsignal.jp/products/primary-antibodies/phospho-rpa32-rpa2-ser8-antibody/83745.

## Eukaryotic cell lines

Policy information about cell lines

| | |
|---|---|
| Cell line source(s) | IMR90, IMR90 E6E7, and U-2OS cells were provided by Jan Karlseder (Salk Institute), and HT1080 6TG cells by Eric Stanbridge (University of California, Irvine). |
| Authentication | All cell lines were validated by Cell Bank Australia using short tandem repeat profiling as indicated in the Methods sections. |
| Mycoplasma contamination | All cell lines were identified as mycoplasma negative as indicated in the methods section. |

| | |
|---|---|
| Commonly misidentified lines (See ICLAC register) | No commonly misidentified cell lines were used in this study. |

## Animals and other organisms

Policy information about studies involving animals; ARRIVE guidelines recommended for reporting animal research

| | |
|---|---|
| Laboratory animals | Species: Mus musculus<br>Strain: NOD.Cg-Prkdc<scid>IL2rg<tm1Wjl>SzJAusJ (NSG)<br>Sex: females<br>Age: at injection 8.9 ± 0.1 weeks, at tumour sizable for window (5x5) 23.3 ± 1.6 weeks, imaging and treatment starting at 27.6 ± 0.7 weeks of age.<br><br>Mice were kept in standard housing at 21±1˚C with an average humidity of 50%, in 12h day light cycles and fed ad libitum. Cage enrichment was undertaken by supplying the fully plastic IVC cages with papier-mâché domes, feeding trays on the cage floor, and soft tissues as nesting material. |
| Wild animals | No wild animals were used in this study. |
| Field-collected samples | No field collected samples were used in this study. |
| Ethics oversight | Animal experiments were conducted in accordance with the Garvan Institute of Medical Research Animal Ethics Committee (guidelines 19/13) and in compliance with the Australian code of practice for care and use of animals for scientific purposes. This information is contained in the methods section. |

Note that full information on the approval of the study protocol must also be provided in the manuscript.